Collagen cross-link profiles and mineral are different between the mandible and femur with site specific response to perturbed collagen

Genevieve E. Romanowicz [a], Aidan H. Terhune [b], Benjamin J. Bielajew [c], Benjamin Sexton [a], Michelle Lynch [a], Gurjit S. Mandair [a], Erin M.B. McNerny [c], David H. Kohn [a,c,*]

[a] *Department of Biologic and Materials Sciences, School of Dentistry, University of Michigan, MI, USA*
[b] *Department of Mechanical Engineering, College of Engineering, University of Michigan, MI, USA*
[c] *Department of Biomedical Engineering, College of Engineering, University of Michigan, MI, USA*

ARTICLE INFO

ABSTRACT

Compromises to collagen and mineral lead to a decrease in whole bone quantity and quality in a variety of systemic diseases, yet, clinically, disease manifestations differ between craniofacial and long bones. Collagen alterations can occur through post-translational modification via lysyl oxidase (LOX), which catalyzes enzymatic collagen cross-link formation, as well as through non-enzymatic advanced glycation end products (AGEs) such as pentosidine and carboxymethyl-lysine (CML). Characterization of the cross-links and AGEs, and comparison of the mineral and collagen modifications in craniofacial and long bones represent a critical gap in knowledge. However, alterations to either the mineral or collagen in bone may contribute to disease progression and, subsequently, the anatomical site dependence of a variety of diseases. Therefore, we hypothesized that collagen cross-links and AGEs differ between craniofacial and long bones and that altered collagen cross-linking reduces mineral quality in an anatomic location dependent. To study the effects of cross-link inhibition on mineralization between anatomical sites, beta-aminoproprionitrile (BAPN) was administered to rapidly growing, 5–8 week-old male mice. BAPN is a dose-dependent inhibitor of LOX that pharmacologically alters enzymatic cross-link formation. Long bones (femora) and craniofacial bones (mandibles) were compared for mineral quantity and quality, collagen cross-link and AGE profiles, and tissue level mechanics, as well as the response to altered cross-links via BAPN. A highly sensitive liquid chromatography/mass spectrometry (LC-MS) method was developed which allowed for quantification of site-dependent accumulation of the advanced glycation end-product, carboxymethyl-lysine (CML). CML was ~8.3× higher in the mandible than the femur. The mandible had significantly higher collagen maturation, mineral crystallinity, and Young's modulus, but lower carbonation, than the femur. BAPN also had anatomic specific effects, leading to significant decreases in mature cross-links in the mandible, and an increase in mineral carbonation in the femur. This differential response of both the mineral and collagen composition to BAPN between the mandible and femur highlights the need to further understand how inherent compositional differences in collagen and mineral contribute to anatomic-site specific manifestations of disease in both craniofacial and long bones.

1. Introduction

Complex structures, such as bones, rely on a multitude of morphological and compositional properties to impart the high strength and resilience required for daily function. Bones are composite materials, primarily comprised of fibrillar type I collagen (organic phase, ~35–45 % by volume), carbonated hydroxyapatite crystals (mineral phase, ~35–45 % by volume), and water (~15–25 % by volume) (Currey,

1989; Mueller et al., 1966). Compromises to either the amount or composition of collagen or mineral in bone can alter both homeostasis and healing. A variety of diseases exhibit features of altered collagen (concentration and ratios of cross-links or glycation products) as well as bone mineral density (BMD), impaired healing, and reduced bone strength (increased fragility) (Daley et al., 2010; Marin et al., 2018; Inzana et al., 2013; Zofkova et al., 2017). Mineral density decreases at different rates in the craniofacial and long bones with disease (Lee et al., 2019). The impact of systemic skeletal disease on composition may therefore be anatomic site-specific, especially between craniofacial and long bones due to differences in embryonic origin (Chung et al., 2004), turnover rate (Huja et al., 2006), and loading (Tsouknidas et al., 2017; Edwards et al., 2014). A limited number of studies (Sasaki et al., 2010; van den Bos et al., 2008), however, have investigated differences in subsets of collagen cross-links between the mandible and femur, and none have related cross-link changes to changes in mineral quality metrics, such as mineral composition and tissue-level mechanics, between anatomic sites. Nor has an expanded collagen cross-link and non-enzymatic glycation profile (including carboxymethyl-lysine (CML)) been compared between craniofacial and long bones. Understanding mechanical changes and their relationship to compositional changes is also important for understanding pathological progression and differential effects of disease in long bones vs. craniofacial bones.

Type I collagen is assembled as fibrils and acquires post-translational, covalent modifications via the family of enzymes lysyl hydroxylases (LH) and lysyl oxidase (LOX) (Smith-Mungo and Kagan, 1998; Trackman, 2016), or via non-enzymatic formation of advanced glycation end products (AGEs). While numerous AGEs have been detected in bone collagen, pentosidine (PEN) is the predominantly reported AGE in (Saito et al., 2006; Wang et al., 2002; Katayama et al., 1996; Kawamura et al., 2019; Saito et al., 2010; Saito et al., 2006; Viguet-Carrin et al., 2006; Chavarry et al., 2019; Odetti et al., 2005; Vaculík et al., 2016; Kida et al., 2019; Hunt et al., 2018; Hunt et al., 2019; Heveran et al., 2019), yet present in low quantities compared to other AGEs (Thomas et al., 2018). CML is of recent interest (Thomas et al., 2018; Creecy et al., 2021; Arakawa et al., 2020; Sroga and Vashishth, 2021; LLabre et al., 2022) but direct quantification of CML between anatomical sites remains a critical knowledge gap. For enzymatic cross-links, LH and LOX control tissue-specific patterning (Hanson and Eyre, 1996; Knott and Bailey, 1998). In bone, the predominant immature enzymatic cross-links are the divalent cross-links, hydroxylysinoketonorleucine (HLKNL) and lysinoketonorleucine (LKNL), which form from available lysine and hydroxylysine groups. HLKNL and LKNL are unstable during processing of tissues for quantification, therefore they are chemically reduced using sodium borohydride to form dihydroxylysinonorleucine (DHLNL) and hydroxylysinonorleucine (HLNL), respectively, which are referenced in literature. Mature, trivalent cross-links form spontaneously from either the HKLNL or LKNL cross-links with an available allysine or hydroxyallysine group. The predominant mature cross-links are hydroxylysylpyridinoline (PYD), lysylpyridinoline (DPD), and pyrroles (Pyr). The non-enzymatic AGEs also form either cross-links or adducts from lysine and hydroxylysine side groups, however, their formation is via glycation or oxidative stress and may affect bone mechanics differently. Some studies (Sasaki et al., 2010; van den Bos et al., 2008) have suggested that the cross-link profile of long bones differ from that of craniofacial bones, yet comparisons of cross-link and select AGE profiles have not been established.

While individual type I collagen cross-links and AGEs are assumed to be similar between long bones and craniofacial bones, this has not been extensively explored. Factors that influence cross-link ratios such as turnover rate, collagen percentage, and total mineral content may differ between bones (Sasaki et al., 2010; Matsuura et al., 2014) and therefore could alter collagen cross-links and AGEs. Differences between long bones and craniofacial bones are often not considered when studying diseases or therapies targeting bone. However, if the composition (e.g. mineral/collagen ratio, percent cross-links, cross-link or AGE profile) is

different between long and craniofacial bone, the respective tissues may resorb or form bone differently in response to disease, therapy or mechanical loading. The impact of different composition and anatomic site-dependence of response to such perturbations has not been investigated, contributing to a gap in knowledge about differential structure-function relations between long bone and craniofacial sites. More specifically, the contribution of collagen cross-links to mechanical properties and mineralization has not been measured in craniofacial bones.

We hypothesized that collagen cross-links and AGEs differ between craniofacial and long bones and that altered collagen cross-linking reduces mineral quality in an anatomic location dependent manner. This hypothesis was tested in a murine model system with multiple levels of anatomic comparisons as well as dose-dependent inhibition of enzymatic cross-linking via beta-aminoproprionitrile (BAPN) (McNerny et al., 2015a; Hammond and Wallace, 2015; McNerny et al., 2015b). This model directly tests the effects of enzymatic cross-links on mineralization and tissue level mechanics as well as the effects of cross-link inhibition among several anatomical sites with inherently different collagen and mineral composition.

2. Methods

2.1. Animal model

Details of the animal model and experiment were previously reported (McNerny et al., 2015a) with analysis of the tibia only. The work reported here adds extensive new collagen compositional, histomorphometric, Raman spectroscopy analysis, and tissue level mechanical analysis of the femur and the mandible, as well as ultra-high performance liquid chromatography analysis of cross-links with tandem mass spectrometry. All animal procedures were approved by the Institutional Animal Care & Use Committee (IACUC) at the University of Michigan. In brief, five-week old, male C57BL/6 mice (Charles River) were weight matched and assigned to treatment groups (±BAPN). Bones analyzed in this study were from subsets of the original $n = 20$ mice/group. Numerous techniques used were destructive, and the sample size for each outcome measure is listed in the respective Methods section. Daily subcutaneous injections of sterile phosphate buffered saline (PBS) or 350 mg/kg Beta-aminoproprionitrile fumarate salt (BAPN) (CAS: 2079-89-2, Sigma Aldrich, St. Louis, MO, USA) were administered daily over 21 days. This method of BAPN delivery has been shown to be a dose-controlled model of lathyrism (Hammond and Wallace, 2015; McNerny et al., 2015; Shen et al., 2018; Li et al., 2013; English et al., 2015; Hammond et al., 2016). Since BAPN only affects newly deposited tissue, growing mice were used for this study to generate a sufficient volume of cross-link inhibited tissue. To provide labelling for dynamic histomorphometric analysis and discriminating newly deposited tissue (cross-link deficient) from existing tissue (normal cross-links), weekly fluorochrome injections were administered on days 1 (alizarin complexone (Alizarin-3-methyl-iminodiacetic acid), 25 mg/kg, Sigma A3882), 7 (calcein, 15 mg/kg, Sigma C-0875), 13 (xylenol orange, 90 mg/kg, Sigma 398187) and 19 (tetracycline hydrochloride, 25 mg/kg, Sigma T3383). Mice were sacrificed at 8 weeks of age by CO_2 inhalation (experimental day 22). Left and right femora and mandibles were harvested, cleaned of soft tissue, and stored frozen in gauze soaked in calcium buffered PBS (McNerny et al., 2015a,b).

2.2. Micro-CT

Left hemimandibles (7–8/group) and left femora (6/group) were scanned by micro-computed tomography (μCT) over the entire length (μCT100 Scanco Medical, Bassersdorf, Switzerland). Scan settings were: voxel size 12 μm, 70 kVp, 114 μA, 0.5 mm AL filter, and integration time 500 ms. Scans were reoriented using Scanco IPL to obtain reproducible volumes of interest (VOI). A 360 μm standard VOI was taken from the mid root of the first mandibular premolar for interradicular bone, and

then rotated 90 degrees to achieve cortical bone sections at the buccal bone of the first molar. Femoral trabecular bone structure was analyzed using a 600 μm thick volume of interest 2.8 mm below the distal end of the femoral epiphysis. Distal cortex was measured at 6 mm from the distal end of the epiphysis for a 360 μm thick volume of interest. Bone volume/total volume (BV/TV) and tissue mineral density (TMD) were calculated for the mandibular cortex, interradicular bone, femoral cortex and femoral trabecular bone. Trabecular number (Tb.N), spacing (Tb.Sp) and thickness (Tb.Th) were also calculated. The VOI analyzed for micro-CT corresponded to the region of interest (ROI) for Raman spectroscopy, histomorphometry, and nanoindentation. All micro-CT analysis was performed using the manufacturer's evaluation software, and a fixed global threshold of 18 % (180 on a grayscale of 0–1000) was used to segment bone from non-bone.

2.3. Collagen cross-link analysis

Sample preparation for direct measures of collagen cross-linking was conducted as described (McNerny et al., 2015a,b). Cross-link quantification was performed using ultra-high performance liquid chromatography with tandem mass spectrometry (LC-MS) and adapted from previously described methods (Naffa et al., 2016; Gaar et al., 2020) with modifications to expand the number of cross-links and AGEs detected without the need for ion-pairing or fluorescence detection. The mature cross-links (PYD, DPD, and Pyr), the immature cross-links (DHLNL HLNL), and the AGEs (PEN and CML) were measured from each whole bone specimen, quantified via a standard curve of each cross-link and normalized to the collagen content (hydroxyproline). For collagen cross-link analysis, the right femora ($n = 6$/group), the epiphyses were removed, and the marrow was flushed with PBS. For the right hemimandibles ($n = 5$–6/group), the central incisor, molars, and condyle were removed, and the bone was cleaned with PBS and flushed to remove any marrow. Both bones were then demineralized with 0.5 M ethylene diamine tetracetic acid (EDTA) for 72 h, washed, suspended in TAPSO buffer, chopped, and the resulting collagen was reacted with sodium borohydride to preserve the immature cross-links (McNerny et al., 2015a,b; Bolger et al., 2020). Samples were then digested with TPCK-treated trypsin at 37 °C for 24 h and defatted with 3:1 chloroform: methanol to remove any lipids present in the collagen matrix. The recovered digest was used for the pyrrole colorimetric assay, an additional aliquot of digest was used for hydrolysis, mixing 1:1 with 12 M hydrochloric acid and baked at 110 °C for 24 h. A portion of the hydrolysate was used for the hydroxyproline assay. The remainder was cleaned on an SPE column (Bond Elut-Cellulose, 12102095, Agilent) as described (Bolger et al., 2020) with a 35 mL wash with 8:1:1 (Acetonitrile: Acetic Acid: Water) and methods slightly modified by eluting with 5 mL of LCMS grade water (W64, Fisher). Samples were then lyophilized and resuspended in 0.1 % formic acid (A117-50, Fisher) spiked with pyridoxine (internal standard) as a modification of previous methods (Bolger et al., 2020) adapted for LC-MS (Naffa et al., 2016; Gaar et al., 2020).

Standards for PYD (CAS# 63800-01-1) and DPD (CAS # 83462-55-9) were purchased from BOCSCI, Inc. DHLNL was purchased from Chem-Cruz (sc-207059C) and used to quantify HLNL as well since DHLNL and HLNL only differ by an oxygen and no standard for HLNL is commercially available. Standards for CML (#16483) and PEN (#10010254) were purchased from Cayman Chemical. Pyrrole standard was purchased (Sigma, M78801) and used in a colorimetric assay (McNerny et al., 2015a,b). Individual cross-links as well as grouped values for total mature (PYD + DPD + pyrroles), total pyridinolines (PYD + DPD), total immature (DHLNL + HLNL), and total enzymatic cross-links (total immature + total mature) were calculated. Ratios reported are DHLNL/HLNL, PYD/DPD, (total pyridinolines)/pyrroles, immature/mature, immature/(total pyridinolines), CML/immature, CML/mature. A known mass list (Table 1) was used for extraction of ion chromatograms for quantification as compared to the standard curves for each species of

Table 1

Post-translational modifications of interest with respective chemical formulas, molecular mass, and accurate masses of [M + H] + charged ions of cross-links and AGEs.

Collagen cross-links and AGEs	Formula	Mass (g/mol)	$[M + H]^+$
Pyridoxine (internal standard)	$C_8 H_{11} N O_3$	169.180	170.081
Hydroxylyslnoroluceine (HLNL)	$C_{12} H_{25} N_3 O_5$	291.348	292.187
Dihydroxylyslnoroluceine (DHLNL)	$C_{12} H_{25} N_3 O_6$	307.347	308.182
Hydroxylysylpyridinoline (PYD)	$C_{18} H_{28} N_4 O_8$	428.437	429.198
Lysylpyridinoline (DPD)	$C_{18} H_{28} N_4 O_7$	412.433	413.203
Pentosidine (PEN)	$C_{17} H_{26} N_6 O_4$	378.430	379.209
Carboxymethyl-lysine (CML)	$C_8 H_{16} N_2 O_4$	204.224	205.118

Key: Pyridoxine is the internal standard. Reduced immature cross-links (hydroxylyslnoroluceine (HLNL), dihydroxylysinonorleucine (DHLNL)), mature cross-links (hydroxylysylpyridinoline (PYD), lysylpyridinoline (DPD)), and select advanced glycations end products (pentosidine (PEN) and carboxymethyl-lysine (CML)).

cross-link.

LC-MS (Agilent 6545 LC/Q-TOF) conditions were adapted from Naffa et al. (Naffa et al., 2016; Gaar et al., 2020) and as follows: injection *v*olume: 20 μL, gradient elution program: Solvent A, 100 % water/0.1 % formic acid (v/v); solvent B, 100 % acetonitrile/0.1 % formic acid (v/v). Gradient: 0 min 90 % solvent B, 2 min 84 % solvent B, 12 min 42 % solvent B and 17 min 10 % solvent B. Run time was 17 min and flow rate was 0.4 mL/min followed by 4 min of column equilibration time (total run time 21 min), column temp: 25°C.

The mass spectrometer used was the MS Q-TOF equipped with dual Jet Stream Technology Ion Source (AJS) Electrospray Ionization Spectrometry (ESI). Positive ion mode was used in all runs. System parameters were: column temperature, 35°C; sheath gas (N2) temperature: 320°C, flow: 10 L/min; Positive ion mode was used with a mass range of 50–1200 *m/z*, scan rate: 2 spectra/s. Tandem mass spectrometry (MSMS) was utilized for CML compound validation (Supplemental Fig. S1), with a scan rate of 4 spectra/s, and a mass range of 50–600 m/z. MSMS was targeted for the mass of CML, at the respective elution time determined by injection of the CML standard. Collision energies for MSMS were 20 and 40 *V*. All data were processed using Thermo Xcalibur 3.0 software. Agilent MassHunter Workstation Qualitative Analysis software version B.06.01 SP1 (Agilent Technologies, Santa Clara, CA, USA) was used for qualitative analysis and quantitation. Three immature cross-link data points in the femur were below the detection limit and excluded.

2.4. Histomorphometry

Additional right femora ($n = 5$–7) and hemimandibles ($n = 6$–7) were prepared for dynamic histomorphometry. In brief, bones were freshly embedded in poly-methyl-methacrylate (PMMA) (Koldmount, SPI Supplies), longitudinally sectioned with a low speed diamond saw blade (IsoMet™, Buehler, Lake Bluff, IL), ground to the region of interest using course grit sandpaper then polished with a series of fine-grit sandpaper as described (Sinder et al., 2013) resulting in half of the bone remaining encased in PMMA with adequate thickness (>2 mm) for subsequent Raman spectroscopy and nanoindentation. The fluorescent labels were visualized using a confocal microscope (Nikon Eclipse T*i* confocal, NY, USA). Images were analyzed for mineral apposition rate (MAR) at 3–5 locations along the ROI and averaged for each site using the Nikon software according to standardized methods (Dempster et al., 2013). The primary goal of the dynamic labeling was to mark areas of new bone formation for the Raman spectroscopy and nanoindentation at areas of BAPN affected tissue.

2.5. Raman spectroscopy, data processing, and spectral analysis

Mineral and matrix composition were measured via Raman

Spectroscopy with a custom built system (Oest et al., 2016) following methods as described (McNerny et al., 2015b; Mandair et al., 2020; Gardinier et al., 2016). In brief, the polished sections used for histomorphometry were also analyzed via Raman (hemimandibles: $n = 7$–8/group, femurs: $n = 8$/group). Regions within the fluorescent labels were probed with a 10×/0.50 NA objective with ~40 mW of laser power at the specimen with an 8-um laser spot (785-nm diode, 25 um slit, spectral resolution of ~4 cm^{-1}). Scans were taken over 4 min and 3 scans were averaged to create a resulting spectrum for one laser spot location. This was then repeated at 3–4 locations per compartment of each bone. Each representative spectra was then individually post processed as described (Mandair et al., 2020). Briefly, spectra were post-processed with a custom MatLab® script which automated unspiking to remove cosmic ray noise and "*adaptive* min-max" polynomial fitting procedure (third order, constrained) to correct for background fluorescence. All spectra were imported into GRAMS/AI software. Linear baselining was applied across known bone Raman spectral regions, followed by normalization against the symmetrical ν_1 phosphate band at ~960 cm^{-1} (ν_1PO$_4$) (Mandair et al., 2020). Select spectral regions were analyzed using standard second derivative and constrained Gaussian deconvolution fitting procedures. The optimum band position centers (approximately ±1–2 cm^{-1}) and heights (minimum of 0, maximum of 1.0) of our deconvoluted curve-fits were determined through an iterative examination of several sets of initial parameters that differed in band position centers and height until consistent results with minimum chi-squared values were obtained. The resulting constrained deconvoluted curve-fit templates were then applied equally to all the spectra and convergence were usually achieved within 5 iterations. Regions analyzed included (sub-bands are listed per range with key bands bolded): 830–900 cm^{-1} (831, **854**, **874**, 890), 900–990 cm^{-1} (923, 940, **958**), 990–1010 cm^{-1} (**1000**), 1010–1100 cm^{-1} (1019, 1028, 1042, **1069**, 1087, 1100), 1200–1400 cm^{-1} (1200, 1221, **1240**, **1263**, 1287, 1309, 1322, 1334, 1335, 1360), and 1560–1714 cm^{-1} (1554, 1569, 1583, 1598, 1613, 1628, 1640, 1649, **1660**, **1679**, 1698). The corresponding peaks of interest were defined (respectively): proline (Pro) at ~853 cm^{-1} (Buckley et al., 2012; Penel et al., 2005) and hydroxyproline (Hyp) at ~876 cm^{-1} (Buckley et al., 2012; Shibata et al., 2013); ν_1 phosphate at ~960 cm^{-1} (Kazanci et al., 2006; Kazanci et al., 2007; Crane et al., 2006); phenylalanine (Phe) at ~1001 cm^{-1} (Penel et al., 2005; Wopenka et al., 2008), carbonate (Carb) at ~1069 cm^{-1} (Awonusi et al., 2007; Taylor et al., 2021), amide I sub-bands at ~1660 cm^{-1} (Gamsjaeger et al., 2017; Chauhan et al., 2018) and ~1679 cm^{-1} (Chauhan et al., 2018); and amide III at 1240 cm^{-1} and 1263 cm^{-1} (Dehring et al., 2006).

Band height ratios were calculated for the following compositional parameters: Mineral/Matrix ratio (~960/1001 cm^{-1}); Carbonate/Phosphate (1069/960 cm^{-1}); Carbonate/Amide *I* (1069/1660 cm^{-1}); Hydroxyproline/Proline (874/854 cm^{-1}); Amide *I* ratio (1660/1679 cm^{-1}); and Amide III (1240/1263 cm^{-1}) ratio. Mineral/Matrix ratio is related to the amount of mineral within a given volume of bone matrix and Mineral/Phenylalanine ratios is positively correlated with ash weight (Taylor et al., 2017) Carbonate/Phosphate ratio measures the degree of *B*-type carbonate substitutions into the bone mineral crystal lattice and is correlated with weight percent carbonate content and mineral crystallinity (Awonusi et al., 2007; Taylor et al., 2021). Mineral crystallinity is the inverse of the full-width at half maximum (1/FWHM) of the Gaussian-fitted ν_1PO$_4$ band at ~960 cm^{-1} and is a measure of bone mineral crystallite size and/or lattice perfection (Awonusi et al., 2007; Taylor et al., 2021; Freeman et al., 2001). Carbonate/Amide *I* ratio is reported to indicate mineral maturity and serve as a mineral/matrix ratio (McCreadie et al., 2006; de Souza et al., 2012). The amide I ratio was extrapolated from earlier spectroscopic studies (Gamsjaeger et al., 2017; Chauhan et al., 2018) and reflects the secondary structure of collagen. Hydroxyproline/Proline ratio is used as indirect measure of

post-translational modifications to bone collagen (Burke et al., 2016). The Amide III 1240/1263 cm^{-1} ratio can provide information into the organization of collagen fibrils in bone. All reported peaks are from peak height at given wavenumber from processed and baselined spectra (Mandair et al., 2020).

2.6. Nanoindentation

Tissue level mechanical properties were measured (hemimandibles: $n = 6$–8/group, femurs: $n = 5$–7/group) and co-localized with the histomorphometry and the Raman spectroscopic measurements (at 2 separate compartments per bone (i.e., trabecular/woven, or cortical) with 5–8 independent indents averaged per compartment). Samples were prepared just prior to nanoindentation by final polish with a felt pad and 0.25 μm diamond suspension (Electron Microscopy Sciences, 50372-21) for 5 min to create a surface with a root mean square surface roughness of <10 nm as described (Sinder et al., 2013). A Berkovich tip was then loaded at each site at 10 μNs^{-1}, to 1000 μN, then unloaded at 10 μNs^{-1} using a 950 TI TriboIndenter (Hysitron, Minneapolis, MN, USA). Indentations were conducted in a humid state via surface hydration with 100 μL calcium buffered PBS that was dabbed off the surface just prior to indentation and re-applied every 5 indents. Young's modulus and hardness were extracted from the load-displacement curve generated using the Oliver-Pharr method after quartz calibration for determination of the tip area function dependent on indent depth (Oliver and Pharr, 1992).

2.7. Statistics

The study was designed with a power calculation based on the primary outcome of altered mineral with BAPN treatment (carbonate/phosphate via Raman spectroscopy). Using means and variance from previous work (McNerny et al., 2015b) for a two-tailed *t*-test yielded a minimum of $n = 5$. IBM SPSS and GraphPad Prism 9.4 were used for statistical analysis and presentation. Raw data was analyzed for assumptions of normality (Shapiro-Wilk) and homogeneity of variance (Levene). For anatomic site (i.e. mandible v. femur) comparisons, where whole bones were used, tests for bone effects and possible interaction with BAPN treatment effects were made with a generalized linear effect model (GLM). The GLM was fit to a design matrix based on the experimental design to test the repeated comparisons of anatomic sites within an animal while adjusting for differences between animal subjects. GLM model summaries of fixed factor effects and compartment site comparisons (contrasts) are shown for the Raman spectroscopy and LC-MS data. Post-hoc comparisons were made for compartment and bone comparisons (or contrasts). Gaussier-Glass corrections were applied for non-homogeneous data and Tukey's honestly significant difference (HSD) post-hoc contrast (between anatomic compartment) tests were employed. Subsequent *t*-tests (Welch's) were conducted to test for BAPN effect for each bone separately, as the GLM could not create contrasts with less than 2 levels in the factor (PBS or BAPN). Outlier statistical tests (Grubb's) were performed, but none were detected. Results are summarized as the mean ± the standard deviation for each bone compartment. Three sample values were omitted from the immature cross-link quantification due to negative values when quantified and therefore considered "not detected". Where relevant, the non-normal and non-homogenous data is annotated. Linear regressions were performed for the Raman outcomes compared to Young's modulus determined from nanoindentation as well as CML to mature and immature cross-link content. All values of $p < 0.05$ are considered significant; values of $p < 0.1$ are noted as trends. Consistent symbols for significance are denoted in each figure or table and applied throughout with the raw *p*-values presented in tables immediately following graphs or in Supplemental Tables 1–2.

3. Results

3.1. Enzymatic collagen cross-links differ between the mandible and femur and BAPN strongly reduces cross-linking in the mandible

Direct measures of collagen cross-links from whole hemimandibles and femora revealed significant enzymatic collagen cross-link differences between bones (Fig. 1A&C, Table 2). Immature cross-links, DHLNL and total mature cross-links (DHLNL + HLNL), were significantly higher in the femur than in the mandible ($p = 0.01$, GLM, Fig. 1A, $p = 0.01$, GLM, Table 2, respectively), predominantly driven by DHLNL content with the femur containing approximately 30 % more DHLNL mol/mol collagen than the mandible. HLNL did not significantly differ by anatomic site ($p = 0.07$, GLM, Fig. 1B). The DHLNL/HLNL ratio was also significantly higher in the femur compared to the mandible ($p = 0.04$, GLM, Table 2). Pyrrolic (Pyr) cross-links were almost twice as high in the mandible compared to the femur ($p = 0.002$, GLM, Fig. 1C). Total mature cross-links (Pyr + PYD + DPD) and ratio of mature/immature were also significantly higher in the mandible ($p = 0.003$, GLM, Table 2, and $p = 0.0001$, GLM, Table 2, respectively), but the individual pyridinolines were not ($p = 0.18$, GLM, Fig. 1D) ($p = 0.69$, GLM, Fig. E). The (PYD + DPD)/Pyr ratio was significantly increased in the femur compared to the mandible ($p = 0.02$, GLM, Table 2). Total enzymatic cross-links ((PYD + DPD + Pyr) + (DHLNL + HLNL)) were not significantly different between the mandible and the femur ($p = 0.503$, GLM, Table 2).

BAPN caused a significant decrease in the mature cross-links in the mandible: PYD ($p = 0.04$, t-test, Fig. 1D), DPD ($p = 0.03$, t-test, Fig. 1E), and PYD + DPD ($p = 0.03$, t-test, Fig. 1F), but not in the femur. While immature cross-links were not significantly altered by BAPN individually, there was a significant factor effect for BAPN on HLNL content ($p = 0.04$, GLM, Fig. 1B). We had previously reported that the mice in this study had a significant reduction in body weight due to BAPN administration (McNerny et al., 2015a). However, there was no significant difference in whole, mineralized bone weight with treatment ($p = 0.42$, GLM, Table 2).

3.2. Advanced glycation end-products (AGE) profiles are different between the mandible and femur

The AGE product, carboxymethyl-lysine (CML) was significantly increased (~8.3×) in the mandible compared to the femur ($p = 0.0001$, GLM, Fig. 2A). No significant differences in the more historically reported AGE, PEN, were detected between bones ($p = 0.11$, GLM, Fig. 1B). MSMS was used to verify the detection of CML, which was validated by the predominant fragment of 84.08 m/z (Supplemental Fig. S1). In both the standard and the samples, this was the most abundant fragment, which corresponds to fragmentation of CML in
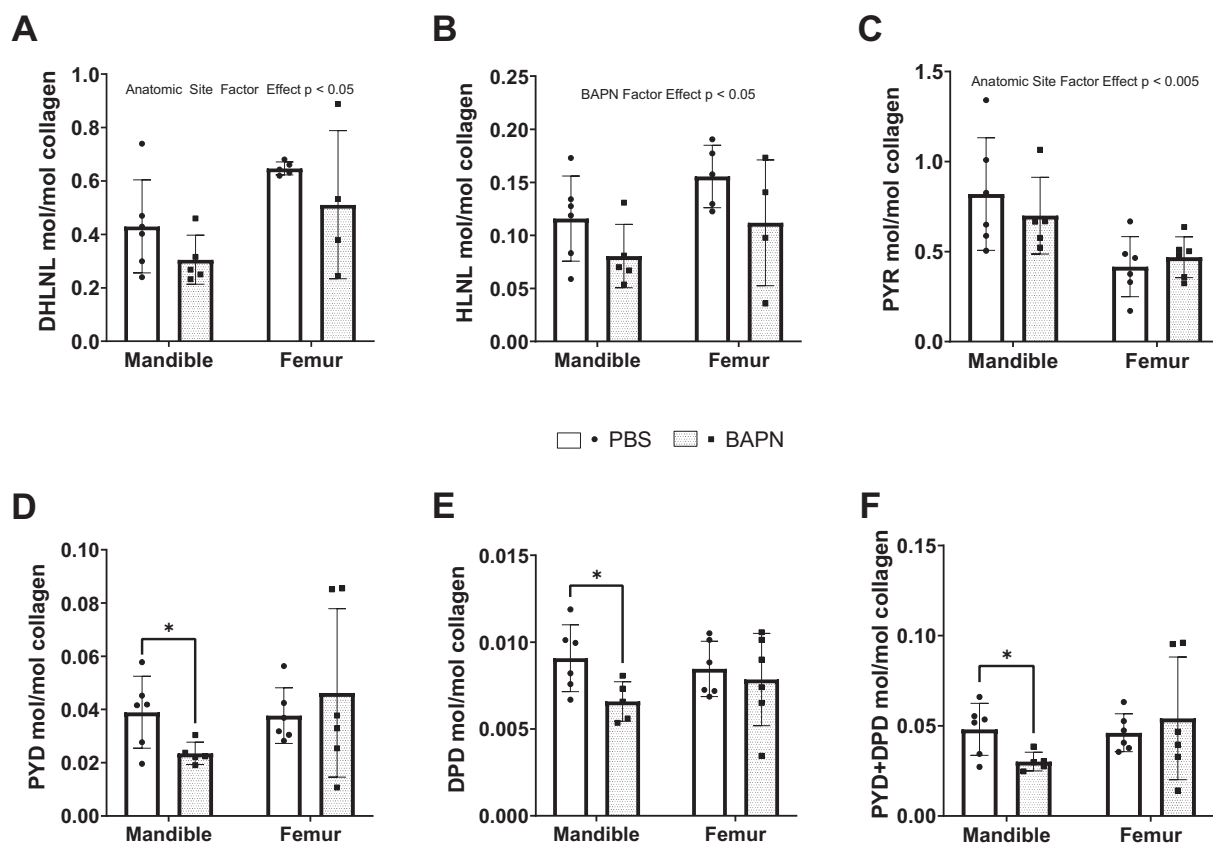

Fig. 1. Differences in enzymatic collagen cross-link between the femur and mandible with BAPN treatment effects. (A) Immature cross-links, DHLNL, were significantly decreased in the mandible compared to the femur ($p = 0.01$, GLM) but not significantly decreased by BAPN ($p = 0.09$, GLM). (B) Immature cross-links, HLNL, were significantly decreased by BAPN overall ($p = 0.04$, GLM), but not by anatomic site ($p = 0.07$, GLM). (C) Pyrrolic cross-links were significantly higher in the mandible compared to the femur ($p = 0.002$, GLM). (D) Mature hydroxylysylpyridinoline (PYD) cross-links were significantly reduced with BAPN treatment in the mandible ($p = 0.04$, t-test), but not the femur. (E) Similarly, mature lysylpyridinoline (DPD) cross-links were reduced by BAPN in the mandible ($p = 0.03$, t-test), but not the femur. (F) The sum of the total mature pyridinoline cross-links (PYD + DPD) was also significantly reduced in the mandible by BAPN ($p = 0.03$, t-test). The interaction term of site and BAPN effects was not significant but is shown in Table 2. Abbreviations: Trivalent mature enzymatic cross-links: hydroxylysylpyridinoline (PYD), lysylpyridinoline (DPD), and pyrroles (Pyr). Divalent immature cross-links: dihydroxylysinonorleucine (DHLNL) and hydroxylysinonorleucine (HLNL). Data are mean ± SD, hemimandible: $n = 5–6$/group, femur: $n = 6$/group. (*$p < 0.05$ as indicated) (Generalized Linear Model (GLM) for repeated measures of anatomic site and treatment effects, Welch's t-test for individual group comparisons for effects of BAPN).

Table 2
Direct measures of collagen cross-link and AGE profile from mandibles and femora as measured by LC-MS.

Site	Mandible		*t*-test	Femur		*t*-test	GLM factor effects (*p*-values)[a]		
	PBS	BAPN	*p*-Value	PBS	BAPN	*p*-Value	Bone	BAPN	Bone * Treat
Mature crosslinks (mol/mol collagen)									
Pyrroles (Pyr)	0.820 ± 0.31	0.700 ± 0.21	0.486	0.465 ± 0.13	0.468 ± 0.11	0.962	**0.002**	0.711	0.348
Hydroxylyslpyridinoline (PYD)	**0.039 ± 0.01**	**0.024 ± 0.004**	**0.038**	0.037 ± 0.01	0.046 ± 0.03	0.518 +	0.184	0.663	0.139
Lyslpyridinoline (DPD)	**0.009 ± 0.002**	**0.007 ± 0.001**	**0.032**	0.008 ± 0.002	0.008 ± 0.003	0.838	0.693	0.071#	0.263
Pyr + PYD + DPD	0.868 ± 0.32	0.730 ± 0.21	0.428	0.510 ± 0.14	0.523 ± 0.12	0.872	**0.003**	0.675	0.288
PYD + DPD	**0.048 ± 0.01**	**0.030 ± 0.005**	**0.028**+	0.045 ± 0.01	0.054 ± 0.03	0.554 +	0.199	0.555	0.136
Immature cross-links (mol/mol collagen)									
Dehydroxylyslnoroluceine (DHLNL)	0.430 ± 0.17	0.305 ± 0.09	0.185	0.648 ± 0.03	0.511 ± 0.28	0.364	**0.011**	0.094#	0.94
Hydroxylyslnoroluceine (HLNL)	0.116 ± 0.04	0.080 ± 0.03	0.138	0.155 ± 0.03	0.112 ± 0.06	0.253	0.067#	**0.044**	0.823
DHLNL + HLNL	0.546 ± 0.21	0.386 ± 0.12	0.172	0.803 ± 0.04	0.623 ± 0.33	0.325	**0.014**	0.075#	0.915
Cross-link Ratios (mol/mol collagen)									
DHLNL/HLNL	3.70 ± 0.40	3.86 ± 0.34	0.322	4.34 ± 1.00	4.90 ± 1.42	0.539	**0.041**	0.3	0.541
PYD/(DHLNL + HLNL)	0.072 ± 0.008	0.063 ± 0.009	0.111	0.040 ± 0.003	0.044 ± 0.009	0.381 +	**<0.0001**	0.327	0.162
DPD/(DHLNL + HLNL)	0.007 ± 0.0008	0.006 ± 0.0009	0.727	0.007 ± 0.001	0.006 ± 0.001	0.359	0.614	0.08#	0.468
(PYD + DPD)/Pyr	0.065 ± 0.03	0.046 ± 0.02	0.293	0.099 ± 0.02	0.124 ± 0.09	0.575	**0.019**	0.62	0.882
PYD/DPD	4.32 ± 1.49	3.60 ± 0.40	0.322	4.69 ± 1.99	5.38 ± 2.32	0.615	0.162	0.974	0.305
(PYD + DPD)/(DHLNL + HLNL)	0.090 ± 0.011	0.081 ± 0.011	0.187	0.050 ± 0.005	0.055 ± 0.011	0.396	**<0.0001**	0.445	0.224
(PYD + DPD + Pyr) + (DHLNL + HLNL)	1.41 ± 0.376	1.12 ± 0.230	0.158	1.26 ± 0.097	1.12 ± 0.352	0.476	0.503	0.135	0.487
(PYD + DPD + Pyr)/(DHLNL + HLNL)	1.75 ± 0.662	2.01 ± 0.657	0.525	0.57 ± 0.084	1.01 ± 0.605	0.198	**<0.0001**	0.154	0.651
Advanced Glycation End Products (AGEs)									
Pentosidine (PEN) (mmol/mol collagen)	0.0101 ± 0.0036	0.0086 ± 0.0024	0.453	0.0077 ± 0.0014	0.0077 ± 0.0021	0.966	0.108	0.699	0.699
Carboxymethyl-lysine (CML) (mol/mol collagen)	0.282 ± 0.21	0.254 ± 0.09	0.766+	0.013 ± 0.004	0.054 ± 0.054	0.127 +	**<0.0001**	0.893	0.477
Whole bone									
Weight	0.018 ± 0.002	0.018 ± 0.002	0.646	0.018 ± 0.005	0.016 ± 0.003	0.521	0.699	0.422	0.421

Significant effects (p < 0.05 or less) in bold, marginally significant denoted with # (p < 0.1).+ (unequal variance)

[a] Generalized linear mixed effect mode (GLM) for main effects of bone and treatment; Subsequent *t*-test (Welch's) for site specific treatment effects.
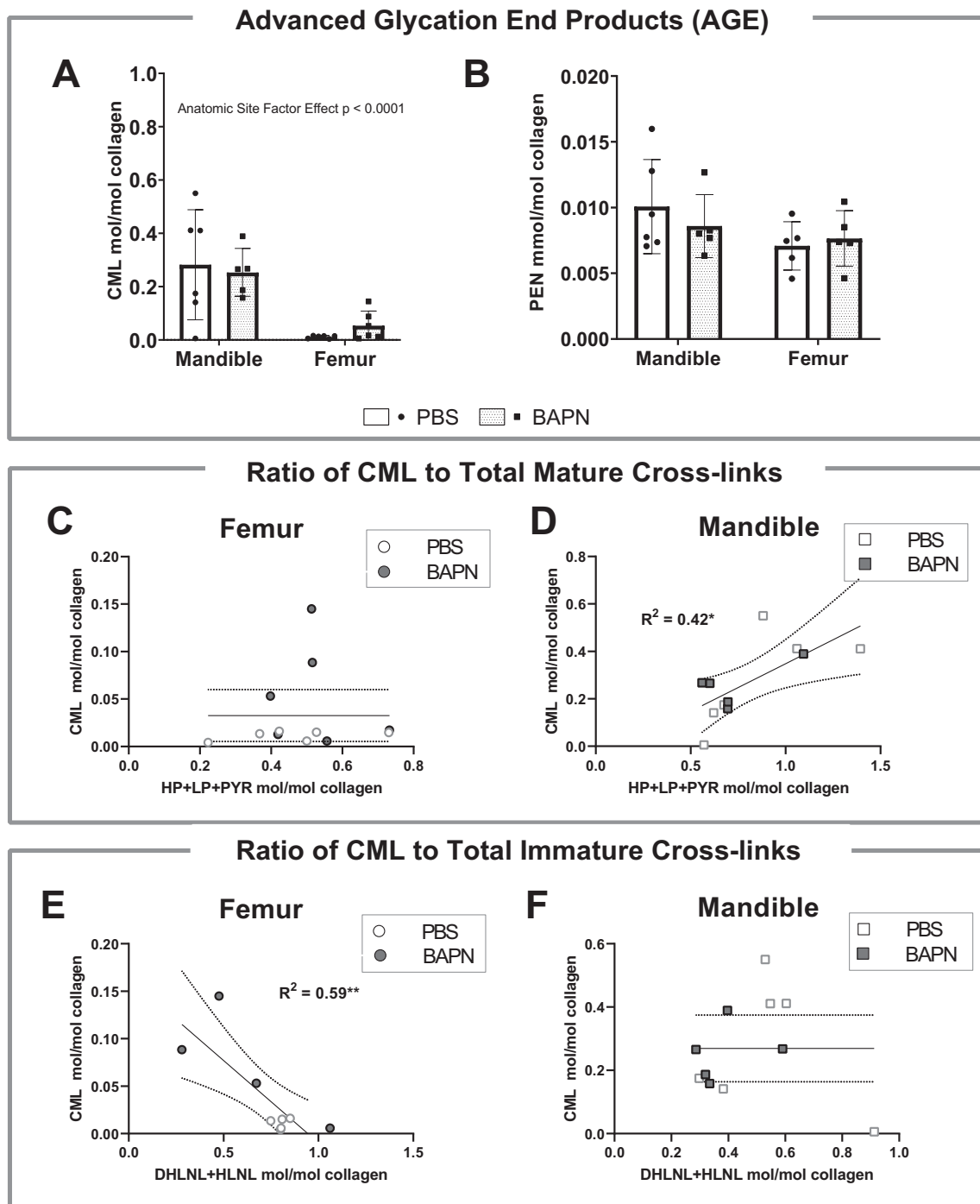
Fig. 2. Advanced glycation end product (AGE) quantification and linear regressions of carboxymethyl-lysine (CML) to the mature and immature cross-links per anatomic site. (A) There were significantly increased levels of CML in the mandible compared to the femur ($p < 0.0001$, GLM). (B) No difference in pentosidine (PEN) was measured ($p = 0.11$) between bones. The ratio of CML to mature cross-links showed no correlation in the femur (C) yet showed a significant positive correlation in the mandible ($p = 0.02$) (D). There was a significant negative correlation of CML to immature cross-links in the femur (E) ($p = 0.01$), but no correlation in the mandible (F). (A–B) Data are mean ± SD, hemimandible: $n = 5$–6/group, femur: $n = 6$/group. (Generalized Linear Model (GLM) for repeated measures of anatomic site and treatment effects, Welch's t-test for individual group comparisons for effects of BAPN). (C–F) For linear regressions, individual data are presented, $n = 11$–12/anatomic site, pooled BAPN and PBS groups, with the linear trend line and 95 % CI and adjusted R^2. (*$p < 0.05$, **$p < 0.01$, as indicated) (Linear Regression Models).

other studies (O'Grady et al., 2020).

Linear regressions were then performed between the CML content and the mature or immature cross-link content to determine if CML competed against enzymatic cross-link formation. There were strong correlations in both the mandible and femur, but with different cross-link subsets and directionality. For the femur, no correlation between

the CML and mature cross-links was detected ($p = 0.89$, Fig. 2C), but a negative correlation between the CML content and the immature cross-link content existed (adj. $R^2 = 0.59$, $p = 0.009$, Fig. 2E). For the mandible, CML positively correlated to total mature cross-links (adj. $R^2 = 0.42$, $p = 0.02$, Fig. 2D), but no correlation was detected between the CML and total immature cross-links ($p = 0.82$, Fig. 2F).
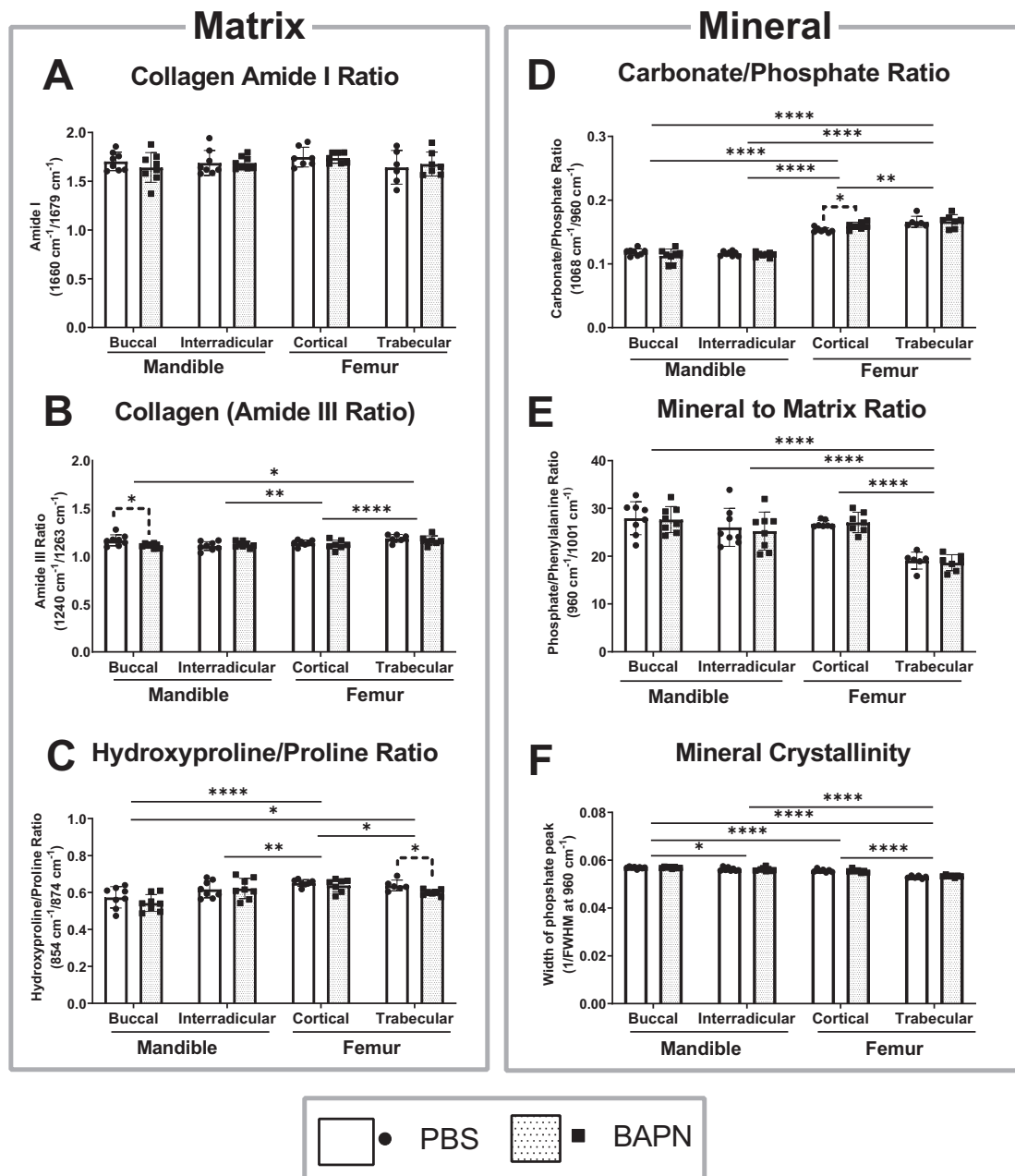
Fig. 3. Anatomic site-specific as well as bone compartment-specific compositional differences between the mandible and femur were measured via Raman Spectroscopy. (A) The Amide I was unchanged between compartments and bones. (B) The amide III ratio was significantly higher in the femoral trabecular bone than the femur cortical bone ($p = 0.0001$, GLM), mandibular buccal cortex ($p = 0.02$, GLM), and mandibular interradicular bone ($p = 0.004$, GLM). BAPN significantly reduced the amide III ratio in the mandible buccal cortex ($p < 0.02$, t-test). (C) Hydroxyproline/proline content was lowest in the mandible buccal cortex compared to the other sites ($p = 0.017$ or less, GLM). BAPN significantly reduced the hydroxyproline/proline ratio in the femur trabeculae ($p = 0.01$, t-test). (D) Carbonate/phosphate ratios were significantly higher in both femoral compartments than the mandibular compartments ($p = 0.003$ or less, GLM) and higher in the femur trabecular than the femur cortical compartment ($p = 0.004$, GLM). BAPN significantly increased carbonate/phosphate in the femoral cortex ($p = 0.02$, t-test). (E) The mineral to matrix ratio was significantly lower in the femoral trabecular compartment ($p < 0.0001$, GLM) than each other compartment. (F) Mineral crystallinity was significantly higher in the mandibular cortex ($p < 0.0001$, GLM) than the femur cortex or trabecular compartments as well as higher than the interradicular bone of the mandible ($p = 0.021$, GLM). Femur cortical bone was significantly higher than the trabecular bone ($p < 0.0001$, GLM). Data are mean ± SD, $n = 6–8$/group. (Generalized Linear Model (GLM) for repeated measures of anatomic site, Welch's t-test for individual group comparisons for effects of BAPN). Full statistical results are shown in Supplemental Table 1. (*$p < 0.05$, **$p < 0.01$, ****$p < 0.001$ as indicated).

3.3. BAPN causes mineral differences in the femur and matrix differences in the mandible

Raman spectroscopy also highlighted differences in mineral and matrix between the mandible and femur (Fig. 3, Table S1). The exception to these differences was the amide I ratio ($p = 0.2$, GLM, Fig. 3A). Amide III ratio was highest in the trabecular compartment as compared

to the femur cortical ($p = 0.0001$, GLM), buccal cortex ($p = 0.02$, GLM) and the interradicular compartment ($p = 0.004$, GLM) (Fig. 3B). Hydroxyproline/proline ratio was highest in the femur cortical compartment compared to the trabecular ($p = 0.017$, GLM) and buccal ($p = 0.0001$, GLM) compartments (Fig. 3C). Mineral differences were seen in numerous Raman band parameters. Carbonate/phosphate was highest in the trabecular compartment compared to the cortex ($p = 0.004$, GLM,

Fig. 4. Dynamic histomorphometry of the mandible and femur. (A) Fluorescent images of longitudinally sectioned mouse femur (cortical and trabecular bone) and mandible (buccal cortical and interradicular) ROIs for analysis via dynamic histomorphometry, nanoindentation and Raman spectroscopy. (B) Schematic of the four fluorophores used to indicate tissue growth during treatment. (C) Mineral apposition rate was significantly different between each compartment (all $p = 0.0001$, GLM) except mandibular interradicular and femur trabecular compartments ($p = 0.09$, GLM). No individual effects of BAPN were detected (t-test). Data are mean $\pm$ SD, hemimandible: $n = 6$–7/group, femur: $n = 5$–7/group. (****$p < 0.0001$ as indicated) (Generalized Linear Model (GLM) for repeated measures of anatomic site, Welch's t-test for individual group comparisons for effects of BAPN). Full statistical results are shown in Supplemental Table 1.
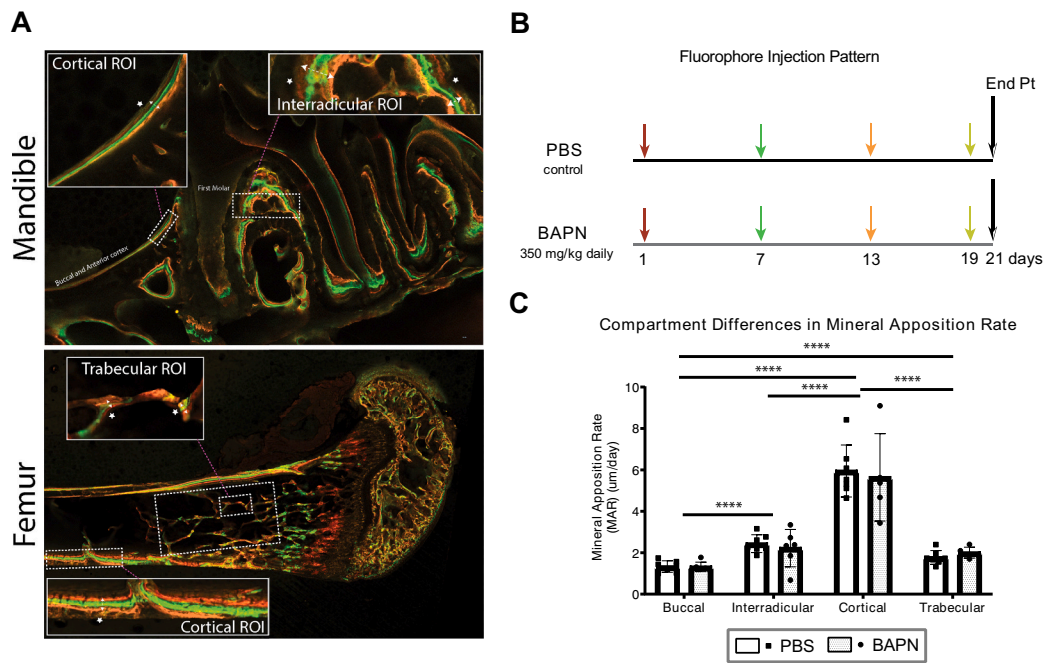
Fig. 3D) followed by the buccal cortex and interradicular bone (both $p = 0.0001$, GLM, Fig. 3D). Mineral to matrix, or mineral/phenylalanine, was lowest in the femur trabecular compartment (all $p < 0.0001$, Fig. 3E). Mineral crystallinity was higher in the buccal cortex compared to interradicular ($p = 0.02$, GLM, Fig. 3F) and the femur trabecular compartment was lower than all others (all $p = 0.0001$, GLM, Fig. 3F).

BAPN increased carbonate/phosphate ratios in the femoral cortex ($p = 0.02$, t-test, Fig. 3D) and decreased the hydroxyproline/proline ratio in the femoral trabecular compartment ($p = 0.01$, t-test, Fig. 3C). BAPN caused a decrease in the Amide III ratio in the mandibular buccal cortex ($p = 0.2$, t-test, Fig. 3B).

3.4. Mineral apposition rate (MAR) and total mineral density (TMD) are anatomical site- and compartment dependent

Both the mandible and femur exhibited compartment-dependent MARs (Fig. 4), allowing for comparison of MAR dependent effects of cross-link inhibition. The ROIs are highlighted in Fig. 4A with the study design and timing of fluorophore injections (Fig. 4B). Typically, the femur would not be considered to have an area of high-MAR, however, the cortical region at the distal epiphysis was primarily new tissue after the 21 days of this study due to the mice being young and growing (Fig. 4C). Likewise, the interradicular bone of the first molar had a relatively high-MAR (Fig. 4C). The trabecular compartment of the distal epiphysis of the femur as well as the mandibular buccal cortical near the first molar showed areas of lower-MAR (Fig. 4C). Each site was significantly different than the other (all $p = 0.0001$, GLM) except for the femoral trabecular vs. mandibular cortical comparisons ($p = 0.09$, Fig. 4C). There was no significant effect of BAPN treatment on MAR (all greater than $p = 0.23$, GLM, Fig. 4C).

3.5. Tissue level Young's modulus and hardness were higher in the mandible as compared to the femur but were not altered by BAPN treatment

Both the mandibular cortex and interradicular bone exhibited significantly higher Young's modulus (all less than $p = 0.001$, GLM, Fig. 5A) and hardness (all less than $p = 0.02$, GLM Fig. 5B) compared to both of the femur compartments, but these mechanical properties did

not differ between the corticated buccal bone and the woven interradicular bone (greater than $p = 0.16$, GLM, Fig. 5A & B). No significant effect of BAPN was found on tissue level Young's modulus or hardness (all greater than $p = 0.18$, t-test, Fig. 5A&B). The femoral cortex exhibited significantly higher Young's modulus ($p = 0.0001$, GLM, Fig. 5A) and hardness ($p = 0.003$, GLM, Fig. 5B) compared to the respective trabecular compartments.

The buccal cortex of the mandible had significantly higher TMD than the interradicular woven bone ($p = 0.0001$, GLM, Fig. 5C) and the femoral cortex had a significantly higher TMD than the woven bone trabecular compartment ($p = 0.0001$, GLM, Fig. 5C). Despite the TMD being lower in the mandibular interradicular bone compartment than the femoral cortical compartment ($p = 0.0001$, GLM, Fig. 5C), the Young's modulus and hardness were higher in the mandible interradicular compartment compared to the femoral cortex (Fig. 5A&B). Likewise, despite increased TMD in the mandibular cortex compared to the interradicular compartment (Fig. 5C), no difference in Young's modulus or hardness were seen (all greater than $p = 0.15$, GLM Fig. 5A–B). No effects of BAPN on any micro-CT parameter were observed in either bone or compartment (all greater than $p = 0.14$, t-test, Fig. 5C & Table S1).

3.6. Mineral quantity and crystallinity significantly correlate to Young's modulus in the femur, while mineral apposition rate (MAR) significantly correlates with Young's modulus in both bones

To determine the impact of the altered mineral and matrix parameters as well as MAR on tissue level Young's modulus, linear regressions were carried out for the individual Raman parameters versus Young's modulus (Fig. 6). Significant correlations for the femur were found between Young's modulus and crystallinity (adj. $R^2 = 0.31$, $p = 0.002$, Fig. 6A), mineral/phenylalanine (adj. $R^2 = 0.38$, $p = 0.0003$, Fig. 6C), and mineral apposition rate (adj. $R^2 = 0.22$, $p = 0.02$, Fig. 6E). MAR was the only significant parameter in the regression for the mandible (adj. $R^2 = 0.16$, $p = 0.03$, Fig. 6F) yet had less explanatory power compared to the femur. The mineral/phenylalanine had the highest explanatory power for the tissue level Young's modulus in the femur with a strong positive correlation explaining 38 % of the variance in Young's modulus.
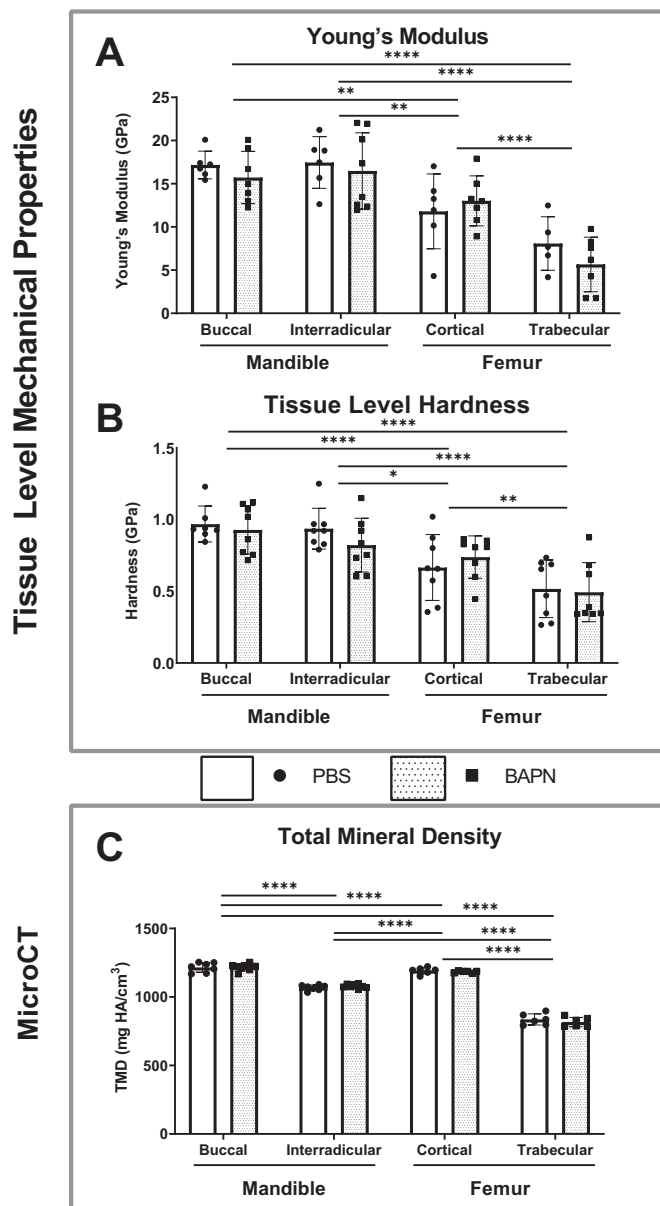
Fig. 5. Tissue level mechanical and Micro-CT outcomes between bone compartments. (A) Young's modulus varied between bones and compartments within the femur. The mandible had a significantly higher Young's modulus than both the femoral cortical and trabecular compartments ($p = 0.001$, or as designated, GLM) and the femoral cortex had a higher Young's modulus than the femoral trabecular bone ($p = 0.0001$, GLM). (B) The same trend was seen with the hardness values ($p = 0.02$, or as designated, GLM). (C) Total mineral density (TMD) was significantly different between every site ($p = 0.0001$, GLM), with decreasing TMD from mandible to femur, with respective cortical compartment higher than woven bone counterpart. No significant effects of treatment were seen in TMD, Young's modulus or hardness (*t*-tests). Data are mean ± SD, (microCT) hemimandible: $n = 5–7$/group, femur: $n = 6$/group, (nanoindentation) hemimandible: n = 6–8/group, femur: 5–7/group. (*p < 0.05, **p < 0.01, ****p < 0.0001 as indicated) (Generalized Linear Model (GLM) and Welch's *t*-test).

4. Discussion

Systemic diseases can alter collagen and mineral, resulting in clinical manifestations that differ between craniofacial and long bones. However, few studies have compared the inherent mineral and collagen compositional differences (including collagen cross-links and AGEs)

between anatomical bone sites. Such comparisons are necessary baseline information to understand the impact of disease-driven composition alterations. Another gap in knowledge is the understanding of anatomical site differences in a state of perturbed collagen cross-linking. This study sought to characterize the anatomic site dependent differences under baseline and perturbed collagen conditions, via thorough characterization of mineral and collagen composition in normal, homeostatic conditions and in the condition of impaired collagen cross-linking via beta aminopropionitrile (BAPN) administration in mice.

Our results showed that numerous collagen compositional differences exist between the mandible and femur. Highlighted in this work are the significantly increased mature/immature cross-link ratio, CML, pyrrolic cross-links (Fig. 1, Fig. 2, Table 2), mineral content (Fig. 3, Fig. 5), Young's modulus, and hardness (Fig. 5) in the mandible compared to the femur. These data comparing the mandible to the femur in mice are similar to the limited human data showing that the mandible has higher mineral content and decreased lysyl hydroxylation (Sasaki et al., 2010). The compositional differences between the mandible and femur were further tested by inhibiting collagen cross-linking where anatomic site-specific differences in mineral and collagen composition were detected (Figs. 1–3, Table 2).

Traditional measures of collagen cross-links and AGEs are cumbersome and have thus limited the widespread application to bone. Advances in LC-MS technology have alleviated some of the technical burden, expanding the detectability of collagen modifications. To our knowledge, this is the first report of anatomic site-specific accumulation of carboxymethyl-lysine (CML) (Fig. 2). Direct measures (LC-MS) of CML in human bone, rat and mouse bone have only recently been reported (Thomas et al., 2018; Creecy et al., 2021; Arakawa et al., 2020; Shirakawa et al., 2016). This study highlights quantification of CML in addition to the more traditionally measured enzymatic and non-enzymatic cross-links, which was not possible using traditional high-performance liquid chromatography with fluorescence detection (HPLC-FLD).

LOX mediated inhibition of enzymatic cross-links via BAPN was more pronounced in the mandible, with a significant decrease in the mature, PYD and DPD cross-links (Fig. 1, Table 2) and a corresponding decrease in the amide III matrix ratio (Fig. 3). Yet, no mineral differences were detected in the mandible with BAPN treatment (Fig. 3). The mature enzymatic cross-link profile did not exhibit a strong BAPN-induced reduction in the femur (Fig. 1). Therefore, disruption of cross-links is not only BAPN dose dependent (McNerny et al., 2015b), but also anatomical site dependent. The femur did show a significant BAPN factor response in the immature cross-link, HLNL (Fig. 1).

While BAPN is generally known to inhibit enzymatic collagen cross-linking systemically, the impairment is limited to newly formed tissue as well as the biodistribution of the drug. We and others have reported inhibition of enzymatic cross-links in the femur and tibia (McNerny et al., 2015a,b; Oxlund et al., 1996; Paschalis et al., 2011). The reductions are often subtle at < 4 weeks of BAPN treatment time, likely due the inability to separate new (affected) bone from old (unaffected) bone, especially when measuring destructively at the whole bone level via HPLC or LC-MS. This is a limitation of a systemically administered drug for which long term treatment can have adverse systemic consequences (Li et al., 2013; English et al., 2015; Miana et al., 2015) and cannot be administered for long enough times to create a large volume of new (cross-link inhibited) tissue. Additionally, most HPLC methods rely on ion-pairing, which strongly impairs the negative ion mode of the mass spectrometry instrument, and therefore would require a dedicated instrument for its use with LC-MS. The LC-MS method here does not use ion-pairing, and is fundamentally different than conventional HPLC-FLD. Therefore, the variance for each analyte may be different from previous studies and unable to detect the subtle changes previously described in the femur.

To determine the effect of collagen cross-link alteration on mineral quantity, composition and mechanical function, compartmental
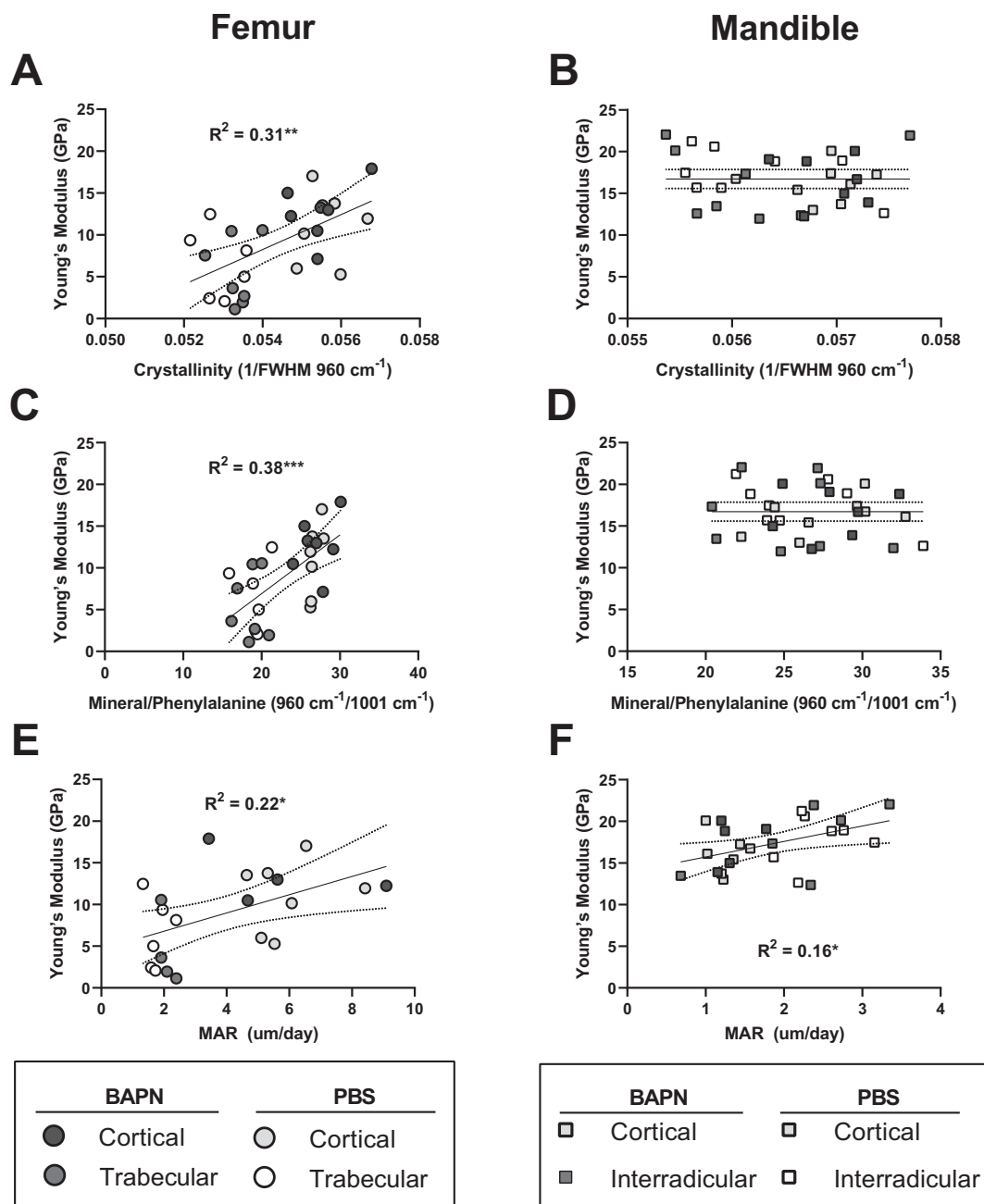
Fig. 6. Linear regressions of mineral and matrix parameters and mineral apposition rate (MAR) to tissue level Young's modulus. Crystallinity, mineral/phenylalanine, and MAR each had significant explanatory power for variation in the Young's modulus in the femur (A,C,E), but only MAR in the mandible (B,D,F). MAR in the femur explained 22 % of the variance in Young's modulus in the femur (E) and 16 % in the mandible (F). Individual data are presented, $n = 5$–6/bone/group, with the linear trend line and 95 % CI and adjusted R^2. (*$p < 0.05$, **$p < 0.01$, ***$p < 0.001$ as indicated) (Linear Regression Models).

properties at the tissue level were compared using Raman spectroscopy and nanoindentation. These compartments included rapidly growing regions of tissue to maximize the effects of BAPN and allow for co-localization of results. In addition to the underlying compositional questions, the comparison of anatomical sites (mandible and femur) was undertaken to investigate differential perturbations to mineral and matrix composition that are common in a variety of systemic diseases (Marin et al., 2018; Burke et al., 2016; Gistelinck et al., 2020). With sequential fluorophore labeling (Fig. 4), we were able to identify tissue at similar levels of maturity to analyze the effect of BAPN treatment. Tissue maturity can impact the amount and quality of mineral, as well as collagen organization (Donnelly et al., 2010; Fuchs et al., 2008; Gourion-Arsiquaud, 2009). Therefore, reduced Young's modulus and

hardness with increased carbonation in the femur compared to the mandible (Fig. 5) are inferred to be inherent differences between the sites, independent of tissue maturity. Additionally, we were unable to detect differences in the amide I (1660/1679 cm^{-1}) ratio between sites or by BAPN, unlike our previous publication (McNerny et al., 2015b). While this study was not powered to detect outcomes in changes in the amide I, numerous other factors can also contribute to a masked effect of BAPN in this ratio which include sample preparation via dehydration (Zhu et al., 2009), tissue age (McNerny et al., 2015b), or orientation (Unal et al., 2021).

An increase in carbonate/phosphate is negatively correlated with fracture toughness and tissue level mechanics (Gourion-Arsiquaud et al., 2009; Unal, 2021) and associated with increased fracture risk

(McCreadie et al., 2006), suggesting that the tissue level mechanical Young's modulus should be inferior in the femur compared to the mandible. This is supported by the nanoindentation data, which showed that the highest Young's modulus was found in both mandibular compartments, followed by the femoral cortex and then the femur trabeculae (Fig. 5). However, Young's modulus was not significantly different between the mandibular compartments despite the interradicular bone having a lower TMD, indicating that the tissue level mechanical properties are relatively homogenous in the mandible. In contrast, the femur had lower Young's modulus in the trabecular compartment compared to the cortical compartment, along with a lower TMD, implying that tissue level mechanical properties are not homogenous in the femur. Differences between the mandible and femur are also highlighted in the regressions which show that Young's modulus has significant positive correlations with crystallinity and mineral/phenylalanine in the femur, but not the mandible (Fig. 6).

In this study, we did not detect any change in tissue level Young's modulus or hardness in the mandible or femur with LOX inhibition via nanoindentation. These techniques yield spatially dependent metrics (Hammond and Wallace, 2015; Paschalis et al., 2011). BAPN also causes changes in whole bone mechanical properties (McNerny et al., 2015a,b; Oxlund et al., 1996; Spengler et al., 1977), but effects are age and dose dependent as well as effected by spatial location. While no nanomechanical changes with BAPN treatment were detected at our discrete testing locations, clear mineral quality changes were found, which should contribute to both whole bone and tissue level mechanical outcomes. Therefore, we speculate that local adaptive changes in the matrix, mineral and matrix interaction, and/or non-collagenous proteins may be occurring to counteract the negative effects of BAPN on tissue level mechanical properties.

Interestingly, we saw trends toward an increase in CML with BAPN ($p = 0.12$, Fig. 2), with a concurrent increase in carbonate/phosphate in the femur (Fig. 2 and Fig. 3). Whereas the mandible did not have a similar CML or carbonate/phosphate response to BAPN (Table 2, Fig. 5 & Table S1). Therefore, higher immature/mature cross-link ratios (such as the femur) may be required for collagen cross-link mediated alterations to mineral composition. CML could be playing a role in the physical interaction between the mineral and collagen (Thomas et al., 2018; Nikel et al., 2012). While we were not able to directly correspond the CML accumulation to the mineral changes as measured via Raman spectroscopy due to the destructive nature of LC-MS, the precise role of CML in mineral/collagen interactions should be further explored.

The mandible has a lower immature cross-link content (Fig. 1). However, enzymatic cross-links have the same lysine and hydroxylysine formation sites as AGEs and therefore can compete with AGE formation (Hudson et al., 2018). The mandible showed increasing CML accumulation with increasing mature cross-linking (Fig. 2), and the femur showed decreasing CML accumulation with increasing immature cross-linking (Fig. 2). One would expect that if the CML accumulation was competing with the mature and immature cross-links, there would be a negative correlation. While it is interesting that there are competing trends between the bones, any explanation would be speculative.

Bones with a higher immature/mature cross-link ratio and low CML accumulation (Fig. 1 and Fig. 2), such as the femur, may be more susceptible to altered mineralization, independent of MAR. Our data provides evidence that altering the cross-link profile can alter mineral in the growing distal femora (Fig. 3), but not in the mandible, which has high levels of mature cross-links and CML (Fig. 2) and high mineral crystallinity (Fig. 3). Additionally, a limitation of this study is that biodistribution of BAPN was not measured, therefore, we are unable to determine if the anatomic site effects are also due to limitations in drug availability.

The mechanism for inherently increased CML in the mandible and trends toward an increase in CML in the femur with BAPN (Fig. 2), remains unexplained. This is a report of anatomic site-dependent accumulation of CML and the first report of CML measured directly from

collagen in bone treated with BAPN. The difference in CML between the mandible and femur could be due to differences in local glucose levels or oxidative stress, both of which alter AGE accumulation (Saito et al., 2006). However, these mechanisms should be further investigated.

Mineral apposition rates between anatomic sites (mandible and femur) and compartments (corticated or woven bone) have not been compared. BAPN impairs collagen cross-links, but it was unknown if treatment with BAPN would also impair the rate at which new tissue was laid down. However, BAPN did not alter the MAR in either bone or compartments (Fig. 4). Since both the femoral cortical compartment and the mandibular interradicular bone had high-MAR, but only the femoral cortex exhibited increased carbonate/phosphate ratios with BAPN treatment, the change in mineral quality via BAPN could not be solely dependent on MAR.

The dependence of tissue level Young's modulus on mineral parameters as well as MAR was further explored with regressions of the co-localized nanoindentation and Raman data. Both the femur and mandible showed MAR dependence on tissue level mechanics (Fig. 6) with 16 % of the variation in Young's modulus explained by MAR in the mandible and 22 % in the femur. No other mineral or matrix variable had explanatory power in the mandible, whereas crystallinity (31 %) and mineral/phenylalanine (38 %) were explanatory in the femora (Fig. 6). Raman parameters such as mineral to matrix, crystallinity, carbonate/phosphate impact tissue level Young's modulus (Akkus et al., 2004; Yerramshetty and Akkus, 2008), but the bulk of these studies were done in long bones and composition-mechanics relationships have not been established in craniofacial bones. The weaker explanatory power of Raman measures in the mandible point to the possibly of different compositional parameters than the traditional Raman metrics of mineral quantity and quality governing tissue level Young's modulus in the mandible.

The bone-dependent compositional response to systemic BAPN highlights that anatomical site comparisons are necessary to understand how altered responses to a variety of perturbations (such as mutations or drug treatment) change between these sites. It is still unknown if the bone-dependent compositional changes are truly a craniofacial vs. long bone phenomenon (ie. purely due to cells of origin, mechanical loading, or other factors) or if similar differences may exist between other less studied anatomical sites compared to the traditionally studied long bones. Additionally, this study focuses on cross-link depleted tissue during normal growth over a short time period (21 days) – essentially homeostatic conditions, and only in male mice. It is also important to understand how cross-links affect tissue between sexes as well as during periods of rapid bone deposition like osseous wound healing.

The implications of these results could extend beyond the findings of compositional differences between anatomical sites and should be explored further to determine the role of altered composition in both health and disease. The detection of CML in mouse bones should be explored further to determine if CML regulates mechanical properties and if it plays a role in mineralization of collagen. If CML can be modulated to determine these effects, it could prove to be a new therapeutic target to modulate tissue level material properties.

5. Conclusion

This study revealed that both mineral and collagen composition, including the AGE, CML, has an anatomical dependence, with a marked increase in the mandible. A differential response of anatomical bone sites to collagen cross-link perturbation was also revealed. In the femur, carbonate/phosphate increased with BAPN treatment, whereas in the mandible this metric did not change. BAPN related matrix changes (both the Raman amide III ratio and the LC-MS mature cross-links) were more pronounced in the mandible compared to the femur. The mandible and the femur also exhibited different collagen cross-link and AGE profiles, mineralization patterns, and tissue level mechanical properties – which highlight the importance of investigating multiple anatomical sites for

bone compositional changes with disease or drug treatment.

Declaration of competing interest

All authors state that they have no conflicts of interest.

Data availability

Data will be made available on request.

CRediT authorship contribution statement

Genevieve Romanowicz: Conceptualization, Methodology, Formal Analysis, Investigation, Writing – Original Draft, Funding acquisition; **Aidan Terhune:** Investigation; **Benjamin Bielajew:** Software, Investigation; **Benjamin Sexton:** Investigation; **Michelle Lynch:** Formal Analysis; **Gurjit Mandair:** Formal Analysis, Writing - Review & Editing; **Erin McNerny:** Methodology, Resources; **David H. Kohn:** Conceptualization, Writing – Review & Editing, Funding acquisition. All authors approve the final version of the manuscript.

Appendix A. Supplementary data

Supplementary data to this article can be found online at https://doi.org/10.1016/j.bonr.2022.101629.

References

Akkus, O., Adar, F., Schaffler, M.B., 2004. Age-related changes in physicochemical properties of mineral crystals are related to impaired mechanical function of cortical bone. Bone 34 (3), 443–453. https://doi.org/10.1016/j.bone.2003.11.003.

Arakawa, S., Suzuki, R., Kurosaka, D., Ikeda, R., Hayashi, H., Kayama, T., Ohno, R.I., Nagai, R., Marumo, K., Saito, M., 2020. Mass spectrometric quantitation of AGEs and enzymatic crosslinks in human cancellous bone. Sci. Rep. 10 (1), 18774. https://doi.org/10.1038/s41598-020-75923-8.

Awonusi, A., Morris, M.D., Tecklenburg, M.M.J., 2007. Carbonate assignment and calibration in the raman spectrum of apatite. Calcif. Tissue Int. 81 (1), 46–52. https://doi.org/10.1007/s00223-007-9034-0.

Bolger, M.W., Romanowicz, G.E., Bigelow, E.M., Ward, F.S., Ciarelli, A., Jepsen, K.J., Kohn, D.H., 2020. External bone size identifies different strength-decline trajectories for the male human femora. J. Struct. Biol. 212 (3), 107650 https://doi.org/10.1016/j.jsb.2020.107650.

Buckley, K., Matousek, P., Parker, A.W., Goodship, A.E., 2012. Raman spectroscopy reveals differences in collagen secondary structure which relate to the levels of mineralisation in bones that have evolved for different functions. J. Raman Spectrosc. 43 (9), 1237–1243. https://doi.org/10.1002/jrs.4038.

Burke, M.V., Atkins, A., Akens, M., Willett, T.L., Whyne, C.M., 2016. Osteolytic and mixed cancer metastasis modulates collagen and mineral parameters within rat vertebral bone matrix. J. Orthop. Res. 34 (12), 2126–2136. https://doi.org/10.1002/jor.23248.

Chauhan, S., Khan, S.A., Prasad, A., 2018. Irradiation-induced compositional effects on human bone after extracorporeal therapy for bone sarcoma. Calcif. Tissue Int. 103 (2), 175–188. https://doi.org/10.1007/s00223-018-0408-2.

Chavarry, N.G.M., Perrone, D., Farias, M.L.F., Dos Santos, B.C., Domingos, A.C., Schanaider, A., Feres-Filho, E.J., 2019. Alendronate improves bone density and type I collagen accumulation but increases the amount of pentosidine in the healing dental alveolus of ovariectomized rabbits. Bone 120, 9–19. https://doi.org/10.1016/j.bone.2018.09.022.

Chung, U., Kawaguchi, H., Takato, T., Nakamura, K., 2004. Distinct osteogenic mechanisms of bones of distinct origins. J. Orthop. Sci. 9 (4), 410–414. https://doi.org/10.1007/s00776-004-0786-3.

Crane, N.J., Popescu, V., Morris, M.D., Steenhuis, P., Ignelzi, M.A., 2006. Raman spectroscopic evidence for octacalcium phosphate and other transient mineral species deposited during intramembranous mineralization. Bone 39 (3), 434–442. https://doi.org/10.1016/j.bone.2006.02.059.

Creecy, A., Brown, K.L., Rose, K.L., Voziyan, P., Nyman, J.S., 2021. Post-translational modifications in collagen type I of bone in a mouse model of aging. Bone 143, 115763. https://doi.org/10.1016/j.bone.2020.115763.

Currey, J.D., 1989. In: Biomechanics of Mineralized Skeletons. Skeletal Biomineralization: Patterns, Processes and Evolutionary Trends, pp. 11–25. https://doi.org/10.1029/SC005p0011 vol. 5, American Geophysical Union (AGU).

Daley, E., Streeten, E.A., Sorkin, J.D., Kuznetsova, N., Shapses, S.A., Carleton, S.M., Shuldiner, A.R., Marini, J.C., Phillips, C.L., Goldstein, S.A., Leikin, S., 2010. Variable bone fragility associated with an amish COL1A2 variant and a knock-in mouse model. J. Bone Miner. Res. 25 (2), 247–261. https://doi.org/10.1359/jbmr.090720.

de Souza, R.A., Xavier, M., Da Silva, F.F., de Souza, M.T., Tosato, M.G., Martin, A.A., de Melo Castilho, J.C., Ribeiro, W., Silveira, L., 2012. Influence of creatine supplementation on bone quality in the ovariectomized rat model: an FT-raman spectroscopy study. Lasers Med. Sci. 27 (2), 487–495. https://doi.org/10.1007/s10103-011-0976-0.

Dehring, K.A., Smukler, A.R., Roessler, B.J., Morris, M.D., 2006. Correlating changes in collagen secondary structure with aging and defective type II collagen by raman spectroscopy. Appl. Spectrosc. 60 (4), 366–372. https://doi.org/10.1366/000370206776593582.

Dempster, D.W., Compston, J.E., Drezner, M.K., Glorieux, F.H., Kanis, J.A., Malluche, H., Meunier, P.J., Ott, S.M., Recker, R.R., Parfitt, A.M., 2013. Standardized nomenclature, symbols, and units for bone histomorphometry: a 2012 update of the report of the ASBMR histomorphometry nomenclature committee. J. Bone Miner. Res. 28 (1), 2–17. https://doi.org/10.1002/jbmr.1805.

Donnelly, E., Boskey, A.L., Baker, S.P., van der Meulen, M.C.H., 2010. Effects of tissue age on bone tissue material composition and nanomechanical properties in the rat cortex. J. Biomed. Mater. Res. A 92A (3), 1048–1056. https://doi.org/10.1002/jbm.a.32442.

Edwards, W.B., Schnitzer, T.J., Troy, K.L., 2014. Bone mineral and stiffness loss at the distal femur and proximal tibia in acute spinal cord injury. Osteoporos. Int. 25 (3), 1005–1015. https://doi.org/10.1007/s00198-013-2557-5.

English, S.J., Piert, M.R., Diaz, J.A., Gordon, D., Ghosh, A., D'Alecy, L.G., Whitesall, S.E., Sharma, A.K., DeRoo, E.P., Watt, T., Su, G., 2015. Increased 18F-FDG uptake is predictive of rupture in a novel rat abdominal aortic aneurysm rupture model. Ann. Surg. 261 (2), 395–404. https://doi.org/10.1097/SLA.0000000000000602.

Freeman, J.J., Wopenka, B., Silva, M.J., Pasteris, J.D., 2001. Raman spectroscopic detection of changes in bioapatite in mouse femora as a function of age and in vitro fluoride treatment. Calcif. Tissue Int. 68 (3), 156–162. https://doi.org/10.1007/s002230001206.

Fuchs, R.K., Allen, M.R., Ruppel, M.E., Diab, T., Phipps, R.J., Miller, L.M., Burr, D.B., 2008. In situ examination of the time-course for secondary mineralization of haversian bone using synchrotron fourier transform infrared microspectroscopy. Matrix Biol. 27 (1), 34–41. https://doi.org/10.1016/j.matbio.2007.07.006.

Gaar, J., Naffa, R., Brimble, M., 2020. Enzymatic and non-enzymatic crosslinks found in collagen and elastin and their chemical synthesis. Org. Chem. Front. 7 (18), 2789–2814. https://doi.org/10.1039/D0QO00624F.

Gamsjaeger, S., Robins, S.P., Tatakis, D.N., Klaushofer, K., Paschalis, E.P., 2017. Identification of pyridinoline trivalent collagen cross-links by raman microspectroscopy. Calcif. Tissue Int. 100 (6), 565–574. https://doi.org/10.1007/s00223-016-0232-5.

Gardinier, J.D., Al-Omaishi, S., Morris, M.D., Kohn, D.H., 2016. PTH signaling mediates perilacunar remodeling during exercise. Matrix Biol. 52, 162–175. https://doi.org/10.1016/j.matbio.2016.02.010.

Gistelinck, C., Weis, M., Rai, J., Schwarze, U., Niyazov, D., Song, K.M., Byers, P.H., Eyre, D.R., 2020. Abnormal Bone Collagen Cross-Linking in Osteogenesis Imperfecta/Bruck Syndrome Caused by Compound Heterozygous PLOD2 Mutations. JBMR Plus 5 (3), e10454. https://doi.org/10.1002/jbm4.10454.

Gourion-Arsiquaud, S., Faibish, D., Myers, E., Spevak, L., Compston, J., Hodsman, A., Shane, E., Recker, R.R., Boskey, E.R., Boskey, A.L., 2009. Use of FTIR spectroscopic imaging to identify parameters associated with fragility fracture. J. Bone Miner. Res. 24 (9), 1565–1571. https://doi.org/10.1359/jbmr.090414.

Hammond, M.A., Wallace, J.M., 2015. Exercise prevents β-aminopropionitrile-induced morphological changes to type I collagen in murine bone. Bonekey Rep 4. https://doi.org/10.1038/bonekey.2015.12.

Hammond, M.A., Laine, T.J., Berman, A.G., Wallace, J.M., 2016. Treadmill exercise improves fracture toughness and indentation modulus without altering the nanoscale morphology of collagen in mice. PLoS One 11 (9), e0163273. https://doi.org/10.1371/journal.pone.0163273.

Hanson, D.A., Eyre, D.R., 1996. Molecular site specificity of pyridinoline and pyrrole cross-links in type I collagen of human bone. J. Biol. Chem. 271 (43), 26508–26516. https://doi.org/10.1074/jbc.271.43.26508.

Heveran, C.M., Schurman, C.A., Acevedo, C., Livingston, E.W., Howe, D., Schaible, E.G., Hunt, H.B., Rauff, A., Donnelly, E., Carpenter, R.D., Levi, M., 2019. Chronic kidney

disease and aging differentially diminish bone material and microarchitecture in C57Bl/6 mice. Bone 127, 91–103. https://doi.org/10.1016/j.bone.2019.04.019.

Hudson, D.M., Archer, M., King, K.B., Eyre, D.R., 2018. Glycation of type I collagen selectively targets the same helical domain lysine sites as lysyl oxidase–mediated cross-linking. J. Biol. Chem. 293 (40), 15620–15627. https://doi.org/10.1074/jbc.RA118.004829.

Huja, S.S., Fernandez, S.A., Hill, K.J., Li, Y., 2006. Remodeling dynamics in the alveolar process in skeletally mature dogs. Anat. Rec. A: Discov. Mol. Cell. Evol. Biol. 288A (12), 1243–1249. https://doi.org/10.1002/ar.a.20396.

Hunt, H.B., Pearl, J.C., Diaz, D.R., King, K.B., Donnelly, E., 2018. Bone tissue collagen maturity and mineral content increase with sustained hyperglycemia in the KK-ay murine model of type 2 diabetes. J. Bone Miner. Res 33 (5), 921–929. https://doi.org/10.1002/jbmr.3365.

Hunt, H.B., Torres, A.M., Palomino, P.M., Marty, E., Saiyed, R., Cohn, M., Jo, J., Warner, S., Sroga, G.E., King, K.B., Lane, J.M., 2019. Altered tissue composition, microarchitecture, and mechanical performance in cancellous bone from men with type 2 diabetes mellitus. J. Bone Miner. Res. 34 (7), 1191–1206. https://doi.org/10.1002/jbmr.3711.

Inzana, J.A., Maher, J.R., Takahata, M., Schwarz, E.M., Berger, A.J., Awad, H.A., 2013. Bone fragility beyond strength and mineral density: raman spectroscopy predicts femoral fracture toughness in a murine model of rheumatoid arthritis. J. Biomech. 46 (4), 723–730. https://doi.org/10.1016/j.jbiomech.2012.11.039.

Katayama, Y., Akatsu, T., Yamamoto, M., Kugai, N., Nagata, N., 1996. Role of nonenzymatic glycosylation of type I collagen in diabetic osteopenia. J. Bone Miner. Res. 11 (7), 931–937. https://doi.org/10.1002/jbmr.5650110709.

Kawamura, M., Masaki, C., Shibata, Y., Kondo, Y., Mukaibo, T., Miyazaki, T., Hosokawa, R., 2019. Pentosidine correlates with nanomechanical properties of human jaw bone. J. Mech. Behav. Biomed. Mater. 98, 20–25. https://doi.org/10.1016/j.jmbbm.2019.06.002.

Kazanci, M., Roschger, P., Paschalis, E.P., Klaushofer, K., Fratzl, P., 2006. Bone osteonal tissues by raman spectral mapping: orientation–composition. J. Struct. Biol. 156 (3), 489–496. https://doi.org/10.1016/j.jsb.2006.06.011.

Kazanci, M., Wagner, H.D., Manjubala, N.I., Gupta, H.S., Paschalis, E., Roschger, P., Fratzl, P., 2007. Raman imaging of two orthogonal planes within cortical bone. Bone 41 (3), 456–461. https://doi.org/10.1016/j.bone.2007.04.200.

Kida, Y., Saito, M., Shinohara, A., Soshi, S., Marumo, K., 2019. Non-invasive skin autofluorescence, blood and urine assays of the advanced glycation end product (AGE) pentosidine as an indirect indicator of AGE content in human bone. BMC Musculoskelet. Disord. 20 (1), 627. https://doi.org/10.1186/s12891-019-3011-4.

Knott, L., Bailey, A.J., 1998. Collagen cross-links in mineralizing tissues: a review of their chemistry, function, and clinical relevance. Bone 22 (3), 181–187. https://doi.org/10.1016/S8756-3282(97)00279-2.

Lee, C., Lee, J.H., Han, S.S., Kim, Y.H., Choi, Y.J., Jeon, K.J., Jung, H.I., 2019. Site-specific and time-course changes of postmenopausal osteoporosis in rat mandible: comparative study with femur. Sci. Rep. 9 (1), 14155. https://doi.org/10.1038/s41598-019-50554-w.

Li, J., Li, H., Wang, L., Zhang, L., Jing, Z., 2013. Comparison of β-aminopropionitrile-induced aortic dissection model in rats by different administration and dosage. Vascular 21 (5), 287–292. https://doi.org/10.1177/1708538113478741.

LLabre, J.E., Sroga, G.E., Tice, M.J.L., Vashishth, D., 2022. Induction and rescue of skeletal fragility in a high-fat diet mouse model of type 2 diabetes: An in vivo and in vitro approach. Bone vol. 156, 116302. https://doi.org/10.1016/j.bone.2021.116302.

Mandair, G.S., Oest, M.E., Mann, K.A., Morris, M.D., Damron, T.A., Kohn, D.H., 2020. Radiation-induced changes to bone composition extend beyond periosteal bone. Bone Reports 12, 100262. https://doi.org/10.1016/j.bonr.2020.100262.

Marin, C., Papantonakis, G., Sels, K., van Lenthe, G.H., Falgayrac, G., Vangoitsenhoven, R., Van der Schueren, B., Penel, G., Luyten, F., Vandamme, K., Kerckhofs, G., 2018. Unraveling the compromised biomechanical performance of type 2 diabetes- and roux-en-Y gastric bypass bone by linking mechanical-structural and physico-chemical properties. Sci. Rep. vol. 8 (no. 1) https://doi.org/10.1038/s41598-018-24229-x. Art. no. 1.

Matsuura, T., Tokutomi, K., Sasaki, M., Katafuchi, M., Mizumachi, E., Sato, H., 2014. Distinct characteristics of mandibular bone collagen relative to long bone collagen: relevance to clinical dentistry. Biomed. Res. Int. 2014 https://doi.org/10.1155/2014/769414.

McCreadie, B.R., Morris, M.D., Chen, T.C., Rao, D.S., Finney, W.F., Widjaja, E., Goldstein, S.A., 2006. Bone tissue compositional differences in women with and without osteoporotic fracture. Bone 39 (6), 1190–1195. https://doi.org/10.1016/j.bone.2006.06.008.

McNerny, E.M.B., Gardinier, J.D., Kohn, D.H., 2015. Exercise increases pyridinoline cross-linking and counters the mechanical effects of concurrent lathyrogenic treatment. Bone 81, 327–337. https://doi.org/10.1016/j.bone.2015.07.030.

McNerny, E.M., Gong, B., Morris, M.D., Kohn, D.H., 2015. Bone fracture toughness and strength correlate with collagen cross-link maturity in a dose-controlled lathyrism mouse model. J. Bone Miner. Res. 30 (3), 455–464. https://doi.org/10.1002/jbmr.2356.

Miana, M., Galán, M., Martínez-Martínez, E., Varona, S., Jurado-López, R., Bausa-Miranda, B., Antequera, A., Luaces, M., Martínez-González, J., Rodríguez, C., Cachofeiro, V., 2015. The lysyl oxidase inhibitor β-aminopropionitrile reduces body weight gain and improves the metabolic profile in diet-induced obesity in rats. Dis. Model. Mech. 8 (6), 543–551. https://doi.org/10.1242/dmm.020107.

Mueller, K.H., Trias, A., Trias, A., Ray, R., 1966. Bone density and composition: age-related and pathological changes in water and mineral content. JBJS 48 (1), 140–148.

Naffa, R., Holmes, G., Ahn, M., Harding, D., Norris, G., 2016. Liquid chromatography-electrospray ionization mass spectrometry for the simultaneous quantitation of collagen and elastin crosslinks. J. Chromatogr. A 1478, 60–67. https://doi.org/10.1016/j.chroma.2016.11.060.

Nikel, O., Laurencin, D., Bonhomme, C., Sroga, G.E., Besdo, S., Lorenz, A., Vashishth, D., 2012. Solid state NMR investigation of intact human bone quality: balancing issues and insight into the structure at the organic-mineral Interface. J. Phys. Chem. C 116 (10), 6320–6331. https://doi.org/10.1021/jp2125312.

O'Grady, K.L., Khosla, S., Farr, J.N., Bondar, O.P., Atkinson, E.J., Achenbach, S.J., Eckhardt, B.A., Thicke, B.S., Tweed, A.J., Volkman, T.L., Drake, M.T., 2020. Development and application of mass spectroscopy assays for Nε-(1-Carboxymethyl)-L-lysine and pentosidine in renal failure and diabetes. The Journal of Applied Laboratory Medicine 5 (3), 558–568. https://doi.org/10.1093/jalm/jfaa023.

Odetti, P., Rossi, S., Monacelli, F., Poggi, A., Cirnigliaro, M., Federici, M., Federici, A., 2005. Advanced glycation end products and bone loss during aging. Ann. N. Y. Acad. Sci. 1043 (1), 710–717. https://doi.org/10.1196/annals.1333.082.

Oest, M.E., Gong, B., Esmonde-White, K., Mann, K.A., Zimmerman, N.D., Damron, T.A., Morris, M.D., 2016. Parathyroid hormone attenuates radiation-induced increases in collagen crosslink ratio at periosteal surfaces of mouse tibia. Bone 86, 91–97. https://doi.org/10.1016/j.bone.2016.03.003.

Oliver, W.C., Pharr, G.M., 1992. An improved technique for determining hardness and elastic modulus using load and displacement sensing indentation experiments. J. Mater. Res. 7 (6), 1564–1583. https://doi.org/10.1557/JMR.1992.1564.

Oxlund, H., Mosekilde, L., Ortoft, G., 1996. Reduced concentration of collagen reducible cross links in human trabecular bone with respect to age and osteoporosis. Bone 19 (5), 479–484. https://doi.org/10.1016/s8756-3282(96)00283-9.

Paschalis, E.P., Tatakis, D.N., Robins, S., Fratzl, P., Manjubala, I., Zoehrer, R., Gamsjaeger, S., Buchinger, B., Roschger, A., Phipps, R., Boskey, A.L., 2011. Lathyrism-induced alterations in collagen cross-links influence the mechanical properties of bone material without affecting the mineral. Bone 49 (6), 1232–1241. https://doi.org/10.1016/j.bone.2011.08.027.

Penel, G., Delfosse, C., Descamps, M., Leroy, G., 2005. Composition of bone and apatitic biomaterials as revealed by intravital raman microspectroscopy. Bone 36 (5), 893–901. https://doi.org/10.1016/j.bone.2005.02.012.

Saito, M., Fujii, K., Soshi, S., Tanaka, T., 2006. Reductions in degree of mineralization and enzymatic collagen cross-links and increases in glycation-induced pentosidine in the femoral neck cortex in cases of femoral neck fracture. Osteoporos. Int. 17 (7), 986–995. https://doi.org/10.1007/s00198-006-0087-0.

Saito, M., Fujii, K., Mori, Y., Marumo, K., 2006. Role of collagen enzymatic and glycation induced cross-links as a determinant of bone quality in spontaneously diabetic WBN/Kob rats. Osteoporos. Int. 17 (10), 1514–1523. https://doi.org/10.1007/s00198-006-0155-5.

Saito, M., Marumo, K., Soshi, S., Kida, Y., Ushiku, C., Shinohara, A., 2010. Raloxifene ameliorates detrimental enzymatic and nonenzymatic collagen cross-links and bone strength in rabbits with hyperhomocysteinemia. Osteoporos. Int. 21 (4), 655–666. https://doi.org/10.1007/s00198-009-0980-4.

Sasaki, M., Matsuura, T., Katafuchi, M., Tokutomi, K., Sato, H., 2010. Higher contents of mineral and collagen but lower of hydroxylysine of collagen in mandibular bone compared with those of humeral and femoral bones in human. J. Hard Tissue Biol. 19 (3), 175–180. https://doi.org/10.2485/jhtb.19.175.

Shen, Y., Jing, D., Hao, J., Tang, G., Yang, P., Zhao, Z., 2018. The effect of β-aminopropionitrile on skeletal micromorphology and osteogenesis. Calcif. Tissue Int. 103 (4), 411–421. https://doi.org/10.1007/s00223-018-0430-4.

Shibata, Y., Suzuki, D., Yamada, A., Maruyama, N., Fujisawa, N., Kamijo, R., Miyazaki, T., 2013. "Lysyl oxidase like-2 reinforces unsatisfactory ossification induced by bone morphogenetic protein-2: relating nanomechanical properties and molecular changes", nanomedicine: nanotechnology. Biology and Medicine 9 (7), 1036–1047. https://doi.org/10.1016/j.nano.2013.04.008.

Shirakawa, J.I., Arakawa, S., Tagawa, T., Gotoh, K., Oikawa, N., Ohno, R.I., Shinagawa, M., Hatano, K., Sugawa, H., Ichimaru, K., Kinoshita, S., 2016. Salacia chinensis L. Extract ameliorates abnormal glucose metabolism and improves the bone strength and accumulation of AGEs in type 1 diabetic rats. Food Funct. 7 (6), 2508–2515. https://doi.org/10.1039/c5fo01618e.

Sinder, B.P., Eddy, M.M., Ominsky, M.S., Caird, M.S., Marini, J.C., Kozloff, K.M., 2013. Sclerostin antibody improves skeletal parameters in a Brtl/+ mouse model of osteogenesis imperfecta. J. Bone Miner. Res. 28 (1), 73–80. https://doi.org/10.1002/jbmr.1717.

Smith-Mungo, L.I., Kagan, H.M., 1998. Lysyl oxidase: properties, regulation and multiple functions in biology. Matrix Biol. 16 (7), 387–398. https://doi.org/10.1016/S0945-053X(98)90012-9.

Spengler, D.M., Baylink, D.J., Rosenquist, J.B., 1977. Effect of beta-aminopropionitrile on bone mechanical properties. J. Bone Joint Surg. Am. 59 (5), 670–672.

Sroga, G.E., Vashishth, D., 2021. Controlled formation of carboxymethyllysine in bone matrix through designed glycation reaction. JBMR Plus 5 (11), e10548. https://doi.org/10.1002/jbm4.10548.

Taylor, E.A., Lloyd, A.A., Salazar-Lara, C., Donnelly, E., 2017. Raman and fourier transform infrared (FT-IR) mineral to matrix ratios correlate with physical chemical properties of model compounds and native bone tissue. Appl. Spectrosc. 71 (10), 2404–2410. https://doi.org/10.1177/0003702817709286.

Taylor, E.A., Mileti, C.J., Ganesan, S., Kim, J.H., Donnelly, E., 2021. Measures of bone mineral carbonate content and mineral maturity/crystallinity for FT-IR and raman spectroscopic imaging differentially relate to physical-chemical properties of carbonate-substituted hydroxyapatite. Calcif. Tissue Int. 109 (1), 77–91. https://doi.org/10.1007/s00223-021-00825-4.

Thomas, C.J., Cleland, T.P., Sroga, G.E., Vashishth, D., 2018. Accumulation of carboxymethyl-lysine (CML) in human cortical bone. Bone 110, 128–133. https://doi.org/10.1016/j.bone.2018.01.028.

Trackman, P.C., 2016. Enzymatic and non-enzymatic functions of the lysyl oxidase family in bone. Matrix Biol. 52–54, 7–18. https://doi.org/10.1016/j.matbio.2016.01.001.

Tsouknidas, A., Jimenez-Rojo, L., Karatsis, E., Michailidis, N., Mitsiadis, T.A., 2017. A bio-realistic finite element model to evaluate the effect of masticatory loadings on mouse mandible-related tissues. Front. Physiol. 8 https://doi.org/10.3389/fphys.2017.00273.

Unal, M., 2021. Raman spectroscopic determination of bone matrix quantity and quality augments prediction of human cortical bone mechanical properties. J. Biomech. 119, 110342 https://doi.org/10.1016/j.jbiomech.2021.110342.

Unal, M., Ahmed, R., Mahadevan-Jansen, A., Nyman, J.S., 2021. Compositional assessment of bone by raman spectroscopy. Analyst 146 (24), 7464–7490. https://doi.org/10.1039/D1AN01560E.

Vaculík, J., Braun, M., Dungl, P., Pavelka, K., Stepan, J.J., 2016. Serum and bone pentosidine in patients with low impact hip fractures and in patients with advanced osteoarthritis. BMC Musculoskelet. Disord. 17, 308. https://doi.org/10.1186/s12891-016-1168-7.

van den Bos, T., Speijer, D., Bank, R.A., Brömme, D., Everts, V., 2008. Differences in matrix composition between calvaria and long bone in mice suggest differences in biomechanical properties and resorption: special emphasis on collagen. Bone 43 (3), 459–468. https://doi.org/10.1016/j.bone.2008.05.009.

Viguet-Carrin, S., Roux, J.P., Arlot, M.E., Merabet, Z., Leeming, D.J., Byrjalsen, I., Delmas, P.D., Bouxsein, M.L., 2006. Contribution of the advanced glycation end product pentosidine and of maturation of type I collagen to compressive biomechanical properties of human lumbar vertebrae. Bone 39 (5), 1073–1079. https://doi.org/10.1016/j.bone.2006.05.013.

Wang, X., Shen, X., Li, X., Mauli Agrawal, C., 2002. Age-related changes in the collagen network and toughness of bone. Bone 31 (1), 1–7. https://doi.org/10.1016/S8756-3282(01)00697-4.

Wopenka, B., Kent, A., Pasteris, J.D., Yoon, Y., Thomopoulos, S., 2008. The tendon-to-bone transition of the rotator cuff: a preliminary raman spectroscopic study documenting the gradual mineralization across the insertion in rat tissue samples. Appl. Spectrosc. 62 (12), 1285–1294. https://doi.org/10.1366/000370208786822179.

Yerramshetty, J.S., Akkus, O., 2008. The associations between mineral crystallinity and the mechanical properties of human cortical bone. Bone 42 (3), 476–482. https://doi.org/10.1016/j.bone.2007.12.001.

Zhu, P., Xu, J., Sahar, N., Morris, M.D., Kohn, D.H., Ramamoorthy, A., 2009. Time-resolved dehydration-induced structural changes in an intact bovine cortical bone revealed by solid-state NMR spectroscopy. J. Am. Chem. Soc. 131 (47), 17064–17065. https://doi.org/10.1021/ja9081028.

Zofkova, I., Davis, M., Blahos, J., 2017. Trace elements have beneficial, as well as detrimental effects on bone homeostasis. Physiol. Res. 391–402. https://doi.org/10.33549/physiolres.933454.